Vesicle Structure and Dynamics in a Mixed Surfactant System: Insights from Small Angle and Quasi Elastic Neutron Scattering

ME-MSE Master Materials Science and Engineering

Alberto Centenaro (6313248)

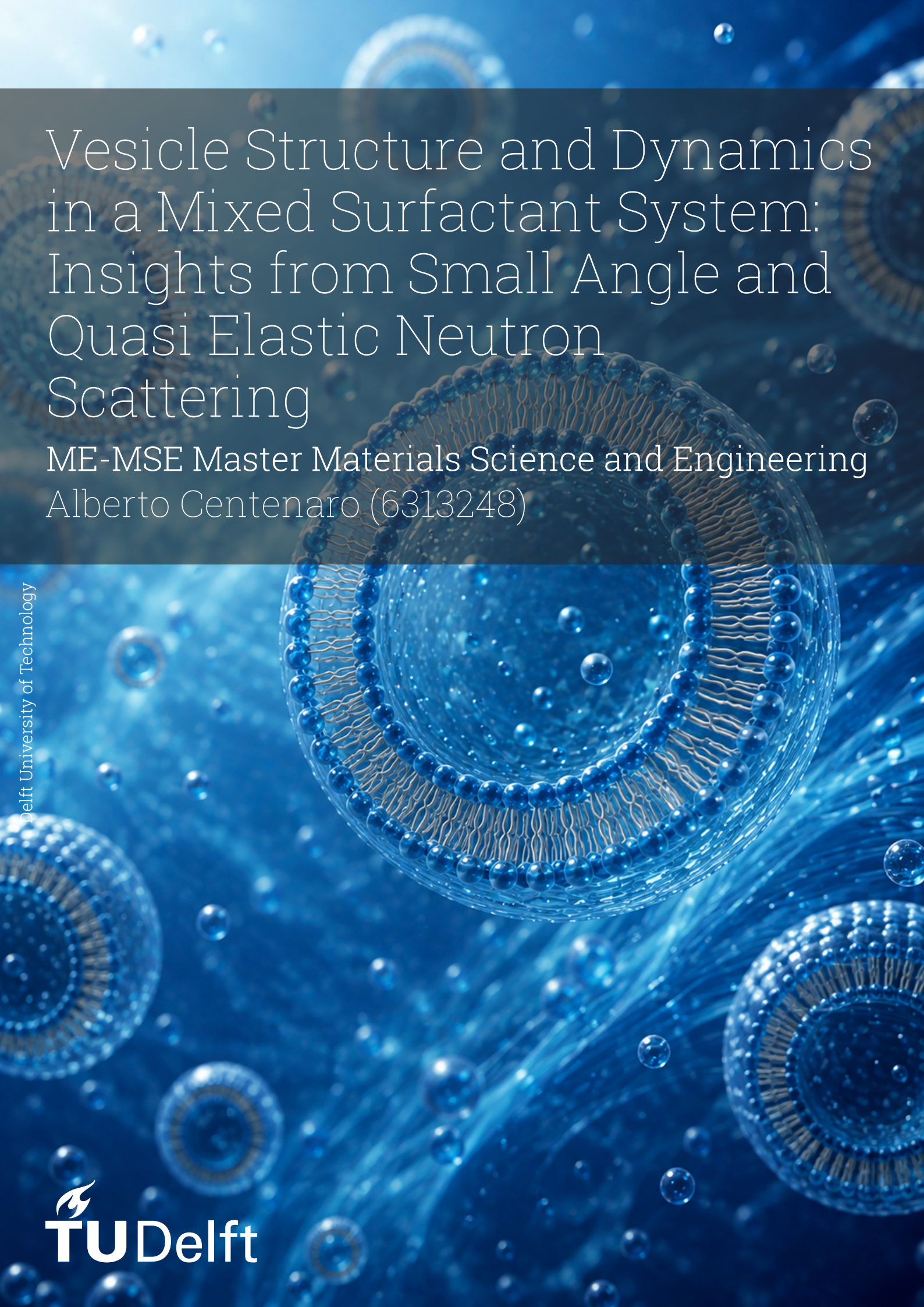

Delft University of Technology

TU Delft

Vesicle Structure and Dynamics in a Mixed Surfactant System: Insights from Small Angle and Quasi Elastic Neutron Scattering

Alberto Centenaro (6313248)

Supervisor: Dr.ir. M.H.F. Sluiter
Supervisor: Dr. T.M. McCoy
Supervisor: Dr. M. Sarter
Supervisor: PhD candidate L. V. Tiihonen

Abstract

This work investigates the internal structuring and molecular dynamics of an aqueous mixed surfactant system composed of the zwitterionic surfactant oleyl amidopropyl betaine (OAPB), and the anionic surfactant sodium bis(2-ethylhexyl) sulfosuccinate (AOT). A key focus of the work is placed on understanding how temperature and ionic strength govern the self-assembly and dynamic behavior of these molecules in situ. Small angle neutron scattering (SANS), quasi elastic neutron scattering (QENS), dynamic light scattering (DLS), and selective deuteration were employed to probe the structure and dynamics across different length and time scales. SANS measurements demonstrate that the OAPB/AOT system undergoes a transition from ellipsoidal micelles to vesicles, driven by electrostatic screening from salt addition. However, increasing the system temperature was found to reverse this transition. In addition, contrast variation through selective deuteration of the surfactants provides insight into their spatial distribution within the vesicle structure. Modelling of the results suggests an asymmetric organization of OAPB and AOT within the vesicle bilayer, with OAPB partitioning preferentially to the inner layer. QENS measurements reveal vesicle Brownian motion, lateral diffusion of surfactants within the membrane and confined localized motions of hydrocarbon chains. These results show that molecular mobility increases with temperature, explaining the observed structural transitions. In addition, the confined motions help explain the small bilayer thicknesses of the vesicles observed by SANS, while the higher apparent immobile fraction of AOT compared to OAPB can be attributed to the asymmetric partitioning of the two surfactants within the bilayer. DLS measurements support the neutron scattering results by providing insight about translational diffusion over different timescales. Overall, this work highlights the capacity for using SANS and QENS as complementary techniques in gaining a deeper understanding of observed structural features and their relationship to the underlying molecular dynamics of soft matter systems.

Acknowledgements

Before the serious part starts, I would like to spend a few words expressing my gratitude. First, I would like to sincerely thank my supervisors, Marcel, Tom, and Mona. Marcel, I know I came to you with a thesis that was supposed to have a computational part, but that plan eventually fell through. Nevertheless, I really appreciated the insight you gave me every time we had a meeting, and how curious and interested you are in topics you may not be familiar with. All the questions you asked really helped me understand whether I truly understood the topic myself. They made me question my knowledge and encouraged me to dive deeper into a subject and make it my own, rather than remaining at the surface level. Mona, a huge part of this thesis would not have been possible without you. You were crucial in helping me familiarize myself with a topic I had never encountered before. You were always patient and willing to help me throughout the learning process, answering every question I had, no matter how small, and I really appreciated that. Tom, I really enjoyed your supervisory approach: treating me as an equal, giving me the right directions I needed to complete this project, and sharing coffee breaks to take a pause from work. I also really appreciated how specific you were with your feedback, never giving general answers but instead providing concrete suggestions that guided me towards writing a more proficient manuscript. And, of course, I enjoyed going out for a pint once in a while. To Lassi and Lucas, thank you for the enjoyable eleven working-day trip to the UK and sharing all those beans. Without you, the workload would have surely buried me, and your help was essential. Lassi, thank you for all the suggestions, tips, and discussions we had about my data, which gave me some great ideas for my work. To Wim, thank you for introducing me to neutron theory after our first meeting about your paper. Without you, I would not have met all these wonderful people. To Eline, thank you for always being available whenever problems came up in the lab, even the smallest ones. You were always there, ready to lend me a hand. Finally, a big thank you to all the friends I met during my Master's at TU Delft and to my family for all the support I received throughout these past two years, both with university-related matters and beyond. Thank you all for helping me enjoy this research period more than I could ever have expected.

Contents

List of Figures

List of Tables

Nomenclature

Abbreviation	Definition
AOT	Sodium bis(2-ethylhexyl) sulfosuccinate (Aerosol-OT)
d-AOT	Sodium bis(perdeutero-2-ethylhexyl) sulfosuccinate (Aerosol-OT-d34)
CMC	Critical Micelle Concentration
DLS	Dynamic Light Scattering
d-OAPB	Perdeutero-Oleyl amidopropyl betaine
E	Ellipsoid
EISF	Elastic Incoherent Structure Factor
FWHM	Full Width Half Maximum
HP	Hayter-Penfold (structure factor)
HS	Hardsphere (structure factor)
MSD	Mean Square Displacement
OAPB	Oleyl amidopropyl betaine
P*	Packing parameter
p	Apparent immobile fraction
QENS	Quasi Elastic Neutron Scattering
SANS	Small Angle Neutron Scattering
SLD	Scattering Length Density
V	Vesicle

1

Introduction

Surfactants are amphiphilic molecules consisting of a hydrophilic headgroup and a hydrophobic tail, and are capable of spontaneously organizing into a wide variety of structures in solution. This dual affinity for water and nonpolar environments drives their accumulation at interfaces, reducing interfacial free energy and upon saturation leads to the formation of self-assembled aggregates such as spherical and ellipsoidal micelles, vesicles, and wormlike micelles [1]. The morphology adopted by surfactants depends on several key factors, including molecular geometry [2], concentration, temperature and the presence of electrolytes and other additives [1]. Their applications range from pharmaceuticals and personal care products, to food processing and advanced materials [3]. Understanding the mechanism governing surfactant self-assembly is essential for their application.

Mixed surfactant systems are of particular interest because the combination of different molecular architectures and properties can give rise to a variety of self-assembled structures [4]. An example of such a system is that comprising the zwitterionic surfactant oleyl amidopropyl betaine (OAPB), which independently forms viscoelastic wormlike micelles in aqueous solution [5], and the anionic surfactant sodium bis(2-ethylhexyl)sulfosuccinate (AOT), which forms prolate ellipsoidal micelles in aqueous solution [6]. Previous studies have shown that when combined these molecules form different self-assembled structures that are responsive to external conditions [7]. OAPB possesses an 18-carbon unsaturated alkyl tail with a single *cis* double bond [7], while AOT has two branched tails attached to a sulfonate group [7]. When AOT is mixed with OAPB in the presence of salt, spontaneous formation of vesicles is observed. This arises from intermolecular interactions, charge shielding and the asymmetry between the mixed headgroup and tail group architectures that lower the spontaneous curvature of the assembly.

Mechanistically, vesicle size is controlled by salt concentration which acts as a screening agent between charged surfactant headgroups, decreasing repulsive forces and enabling lower curvature of the membrane. Surfactant concentration and the AOT to OAPB ratio also play crucial roles in vesicle formation [7]. These results are significant because vesicles are among the most important self-assembled structures formed by amphiphilic molecules, as their bilayer architectures resembles biological membranes and enables encapsulation of hydrophobic and hydrophilic compounds. Consequently, they have attracted interest for many applications including drug delivery and encapsulation [7].

Equilibrium structures of many surfactant systems have been extensively characterized [8],

and small angle neutron scattering (SANS) has become a well established technique for determining the morphology of surfactant aggregates [9]. In contrast, comparatively less is known about the molecular dynamics accompanying self-assembly, and their influence on structural transitions [10]. Understanding these dynamics is essential because they govern key processes such as aggregate stability, micelle lifetimes, and transitions between different morphologies. Molecular motions occur over a broad range of length and time scales, from the translational diffusion of entire aggregates to localized motions, including the lateral diffusion of surfactant molecules within the membrane and conformational fluctuations of the hydrocarbon chains. These dynamic processes are closely coupled to molecular packing and therefore influence the size, shape, and stability of self-assembled structures, as well as their response to external factors such as temperature and ionic strength [10].

The present work aims to investigate the structural and dynamic properties of OAPB/AOT self-assembly in aqueous solution and to determine how salt concentration and temperature influence its dynamics and, consequently, the resulting morphology. Particular attention is devoted to the transition between vesicles and ellipsoidal micelles and the role of electrostatic screening in stabilizing different morphologies. In addition, the use of selective deuteration enables contrast variation experiments that provide insight into the spatial distribution and dynamics of specific surfactants within the aggregates.

Addressing these questions requires complementary experimental techniques capable of probing the different spatial and temporal scales involved in surfactant self-assembly. Small angle neutron scattering (SANS) was therefore employed to determine the morphology of the aggregates, while quasielastic neutron scattering (QENS) was used to investigate molecular motions on the picosecond to nanosecond time scale [10]. In addition, dynamic light scattering (DLS) measurements complemented the neutron scattering experiments by probing the translational diffusion and hydrodynamic size of the aggregates on longer time scales.

2

Theory

2.1. Surfactants and self-assembly

A surfactant (surface-active agent) is a substance that readily adsorbs onto surfaces and interfaces of a system and decreases the free energy [1]. Surfactants are used in a vast array of applications, including food processing, agrochemicals, pharmaceuticals, personal care products, petroleum processing, paint, coatings and many more. [3].

In general, a surfactant's structure can be divided into two main components [1]:

- Lyophobic group: the region of the molecule that has little affinity for the solvent (known as the hydrophobic group when the solvent is water);
- Lyophilic group: the region of the molecule that has a strong affinity for the solvent (called the hydrophilic group if the solvent is water).

There are different classifications for surfactants based primarily on the type of hydrophilic groups present in their chemical structure [1],[11]:

- Anionic: the headgroup possesses a negative charge;
- Cationic: the headgroup possesses a positive charge;
- Zwitterionic: the headgroup contains both positive and negative charges;
- Non-ionic: the headgroup does not bear any formal charge.

When dissolved in water, surfactants can organize into different structures that reduce the system's free energy by minimizing unfavorable interactions. This is achieved through the formation of aggregates, or micelles, in which the hydrophobic tails are directed toward the interior of the aggregate, while the hydrophilic headgroups remain solvated by the surrounding water. This phenomenon is known as self-assembly [1].

The minimum surfactant concentration at which monomeric surfactant molecules start to aggregate and form micelles is known as the critical micelle concentration (CMC) [12]. Below the CMC, surfactants are present predominantly as monomers. Above the CMC, surfactants form micelles to minimize the interfacial free energy [1].

During this micellization process, surfactant molecules may experience a loss of entropy as they transfer from the bulk solution into the aggregate. In the case of ionic surfactants, micelle formation is opposed by electrostatic repulsion between similarly charged surfactants [1].

Consequently, micellization is governed by a balance between opposing forces: unfavorable interactions, such as steric hindrance and electrostatic repulsion, and favorable hydrophobic interactions that reduce the free energy of the system.

Once the CMC is reached, surfactants begin to aggregate and may adopt different morphologies, such as spherical, ellipsoidal, vesicular, elongated cylindrical, or wormlike structures (cylindrical micelles with hemispherical end caps, Fig. 2.1) [13].

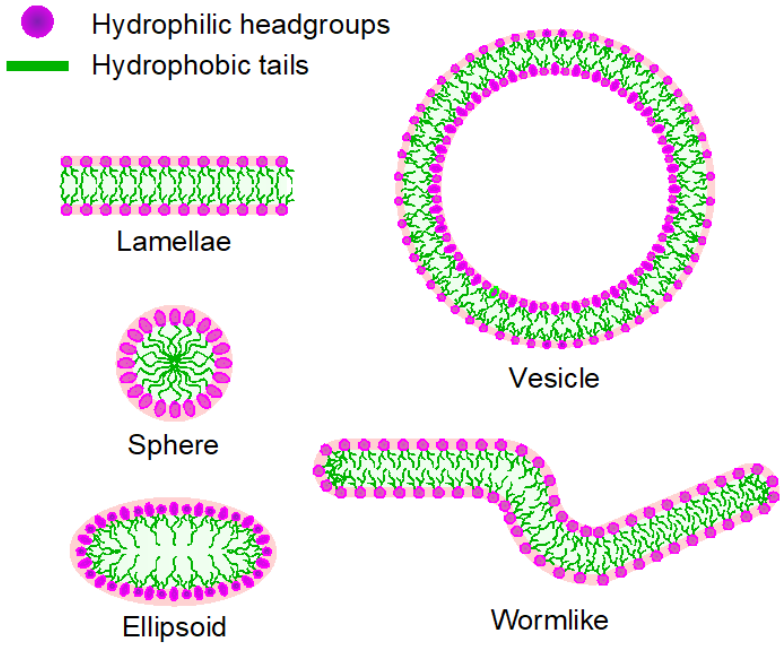

Figure 2.1: Schematic of main micellar structures. Hydrophilic headgroups are shown in pink and hydrophobic tails in green.

2.2. Packing parameter

The process of surfactant aggregation is mainly due to hydrophobic interaction, while the steric and electrostatic repulsion between the headgroups are responsible for the limited size of the aggregates [10]. These aggregates are thermodynamically in equilibrium, but adapt according to changes in the environment. By tailoring molecular architecture, charge, concentration, ionic strength, and other parameters, one can obtain structures with specific size and shape [10]. The shape of micelles can be predicted and quantitatively described by using a geometrical packing parameter (P^*) [1], defined as:

$$P^* = \frac{V_H}{a_0 l_c} \tag{2.1}$$

where V_H is the volume occupied by the hydrophobic group, l_c is the length of the hydrophobic chain and a_0 is the cross-sectional area occupied by the hydrophilic headgroups. Eq. 2.1 provides a numerical value used to predict the micelle shape (Fig. 2.2). From Tanford $V_H = 27.4 + 26.9n$ Å^3, and $l_c = 1.5 + 1.265n$ Å, with n number of carbon atoms in the chain.

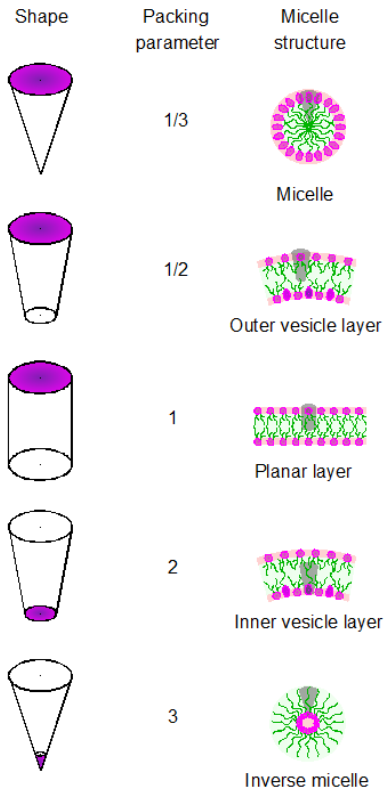

Figure 2.2: Various micellar structures and their corresponding packing parameters (values are from [2]).

By changing the hydrocarbon chain length, or headgroups, the packing parameter can be tuned, leading to the formation of different micellar structures. The value of a_0 depends not only on the structure of the hydrophilic headgroup, but also on the presence of electrolytes, temperature, pH, and other additives. For instance, when electrolytes are added to the solution, charge screening reduces electrostatic repulsion between headgroups, thereby decreasing a_0. This results in an increase in the packing parameter and a consequent change in micelle shape [1].

Therefore, the packing parameter can be considered a useful indicator for predicting an expected micellar structure. However, its application becomes more challenging when additional intermolecular forces are involved, as in mixed-surfactant systems. In these systems, interactions between different surfactant headgroups and hydrophobic interactions arising from diverse tail architectures introduce additional complexity. These interactions can influence all the parameters that determine the value of P^*, making its accurate estimation difficult. Moreover, the packing parameter can vary significantly with solution conditions, further complicating the prediction of micellar morphology when the relevant interactions are not fully understood or well defined [15].

2.3. Small Angle Neutron Scattering (SANS)

Small angle neutron scattering (SANS) is an elastic scattering technique used to probe structures on the nanometer length scale [16]. During measurement, neutrons interact with the atomic nuclei of the sample and are scattered at small angles while conserving their energy (elastic scattering) [17]. The scattered neutrons are collected by a detector, which records

both the scattering angle and the scattered intensity.

The scattering process is described by the scattering vector in Eq. 2.2 [17]

$$Q = k_s - k_i, \tag{2.2}$$

whose magnitude, for elastic scattering, is given by Eq. 2.3

$$Q = \frac{4\pi \sin\theta}{\lambda}, \tag{2.3}$$

where λ is the neutron wavelength and 2θ is the scattering angle (Fig. 2.3).

The measured scattering intensity $I(q)$ is proportional to the differential scattering cross section, which gives the number of neutrons (σ) scattered at a particular solid angle $d\Omega$ [18]:

$$I(q) \propto \frac{d\sigma}{d\Omega}(q) \tag{2.4}$$

For a system of interacting particles, the differential scattering cross section can be written as Eq. 2.5 [17]

$$\frac{d\sigma}{d\Omega}(q) = n(\rho_p - \rho_s)^2 V^2 P(q) S(q), \tag{2.5}$$

where n is the particle number density, $\rho_p - \rho_s$ is the scattering length density (SLD) contrast between the particles (ρ_p) and the surrounding medium (ρ_s), V is the particle volume, $P(q)$ is the form factor, and $S(q)$ is the structure factor.

The form factor $P(q)$ describes the size and shape of individual particles, whereas the structure factor $S(q)$ accounts for spatial correlations arising from interparticle interactions.

In neutron scattering, the SLD is defined as (Eq. 2.6) [19]:

$$SLD = \frac{1}{V} \sum_i b_i, \tag{2.6}$$

where b_i denotes the coherent scattering length of nucleus i. Unlike X-rays, which interact with electron clouds, nuclear scattering lengths vary non-systematically across the periodic table. This property enables contrast variation between isotopes, allowing specific components of a complex system to be selectively highlighted or suppressed.

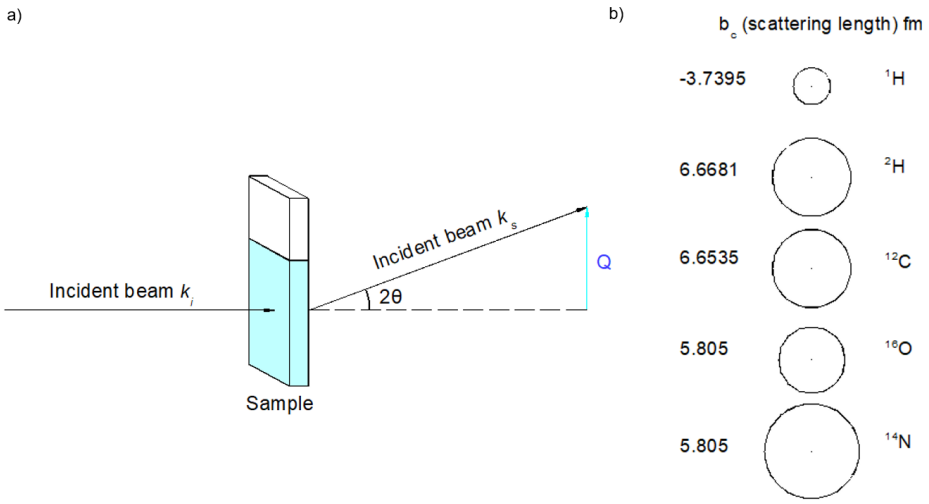

Figure 2.3: a) Schematic representation of the scattering process in SANS and scattering vector, Q b) Coherent nuclear scattering lengths for organic elements and isotopes (data retrieved from [20]).

As deuterium has a larger coherent neutron scattering length than hydrogen (Fig. 2.3), contrast variation is widely used in SANS to probe the structural properties of biological molecules and other organic complex systems [21]. More specifically, by varying the (H_2O/D_2O) ratio, the scattering length density of the solvent can be adjusted to match the SLD of a specific material [22]. Alternatively, selective deuteration can be employed by chemically replacing ^1H atoms with ^2H within the molecular structure, thereby altering the SLD of the material itself [21]. When the SLD of the material closely resembles that of the solvent, the contrast between the two phases is minimized, rendering them indistinguishable.

2.4. Quasi Elastic Neutron Scattering (QENS)

QENS is a technique used to study the dynamics of atoms and molecules in materials of length scales ranging from angstroms to nanometers, and on time scales from picoseconds to nanoseconds [10]. These dynamics appear as a broadening of the elastic line ($\Delta E = 0\,\mathrm{eV}$) [23], which is due to dynamics that are slower than the time resolution associated with the instrument. The technique is based on inelastic scattering between neutrons and nuclei, which results in an energy transfer.

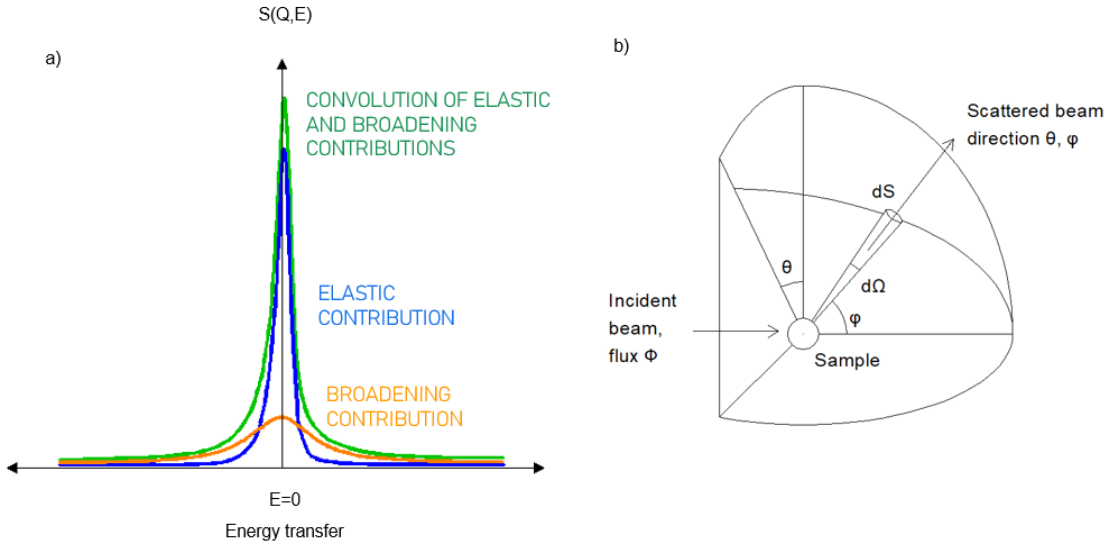

Figure 2.4: a) Schematic representation of a typical QENS spectrum showing the two contributions to the dynamics. Green is the resulting convolution that makes up the full spectrum. b) Conventional schematic representation of the double differential scattering cross section (adapted from [24]).

Fig. 2.4a shows a typical spectrum obtained from a QENS measurement. In a real experiment, the elastic line does not appear exactly at $\Delta E = 0$ eV, but rather with a finite width corresponding to the energy resolution of the instrument, *i.e.* the minimum detectable energy transfer. For IRIS, the energy resolution is $\Delta E = 17.5$ μeV [25]. Consequently, the experimentally measured spectrum comprises a broadened elastic peak that partially overlaps with the quasielastic contribution.

The effective interaction between neutrons and nuclei is quantified by the scattering cross section. The coherent cross section, σ_{coh}, is determined by the average scattering length, $\langle b \rangle$, of the isotopes of a given element and is defined as [26]:

$$\sigma_{\text{coh}} = 4\pi \langle b \rangle^2. \tag{2.7}$$

The incoherent cross section is given by

$$\sigma_{\text{inc}} = 4\pi \left(\langle b^2 \rangle - \langle b \rangle^2 \right). \tag{2.8}$$

Here,

$$\langle b^2 \rangle = \sum_k c_k b_k^2, \tag{2.9}$$

where c_k is the concentration of isotope k. The total scattering cross section σ is therefore the sum of the coherent and incoherent contributions.

The measurable quantity in QENS is the double differential scattering cross section (Fig. 2.4b), defined as the probability that an incident neutron with energy E_0 is scattered into a solid angle $d\Omega$ with an energy transfer between E_0 and E_1. Here, the energy transfer represents

the difference between the initial and final neutron energies exchanged during the scattering process, and can be expressed as [27]

$$E_1 - E_0 = \hbar\omega, \tag{2.10}$$

where ω is the angular frequency associated with the neutron energy exchange and $\hbar$ the reduced Planck constant. Consequently, in inelastic neutron scattering experiments, the scattered intensity is measured as a function of either E or ω.

As mentioned above, neutrons interact with the sample through both coherent and incoherent scattering processes, and the double differential cross section can therefore be written as a weighted sum of the two contributions [10]:

$$\frac{d^2\sigma}{dE, d\Omega} = \frac{\sigma_{\text{coh}}}{4\pi} S_{\text{coh}}(Q, E) + \frac{\sigma_{\text{inc}}}{4\pi} S_{\text{inc}}(Q, E). \tag{2.11}$$

Scattering from systems containing hydrogen is predominantly incoherent, since $\sigma^H_{\text{inc}} = 80.27 \text{ barn} \gg \sigma^{\text{any}}$ [20]. As a result, in QENS experiments the measured signal frequently arises mainly from hydrogen dynamics, allowing hydrogen atoms to act as effective "labels" of molecular motion within a system [26].

In SANS, the experimental Q values are small, resulting in sufficient coherent scattering even for large objects containing many hydrogen nuclei (despite hydrogen having a large incoherent scattering cross section). As Q increases, the coherent scattering decreases rapidly and often becomes much smaller than the incoherent component. Therefore, in QENS, Q values are high relative to SANS (> 0.2 Å^{-1}), scatterers are often small, and their hydrogen content is sufficiently high to make the incoherent scattering dominate over the coherent contribution [28].

2.5. Dynamic Light Scattering (DLS)

Dynamic light scattering (DLS) is a technique based on Brownian motion that probes the temporal fluctuations in the intensity of light scattered by particles as they move through a medium [29]. Since the scattered intensity depends on the motion of the particles, it is directly related to their translational diffusion coefficient. Smaller particles diffuse more rapidly than larger ones, resulting in faster fluctuations of the scattered light intensity [29].

Quantitative information about these dynamics can be extracted using autocorrelation analysis. By monitoring the scattered intensity over different time intervals, an autocorrelation function is obtained that decays exponentially with the delay time, τ, according to Eq. 2.12 [29]:

$$C(\tau) = A \cdot \exp(-DQ^2\tau) + B \tag{2.12}$$

where A is the amplitude of the correlation function, B is the baseline, D is the translational diffusion coefficient, and Q is the magnitude of the scattering vector [29].

3

Materials and methods

3.1. Materials

Oleyl amidopropyl betaine, both in the hydrogenated (OAPB, pure) and deuterated (d-OAPB, isotopic purity, D, 92.6$\pm$ 2$\%$) form together with d-34 Sodium bis(2-ethylhexyl-d17) sulfosuccinate (d-AOT, isotopic purity, D, 97.4$\pm$ 2$\%$) were synthesized by Dr Carl Recsei, National Deuteration Facility, Australian Nuclear Science and Technology Organisation (ANSTO). Sodium bis(2-ethylhexyl-d17) sulfosuccinate (AOT, pure) was obtained from Merck (Darmstadt Germany). Sodium chloride was also obtained from Merck. Deuterium oxide (D_2O, 99.8$\%$ atom D) was from Sigma Aldrich. Fig. 3.1 reports the chemical structure of these surfactants and their key properties in table 3.1.

Table 3.1: Properties coherent and incoherent scattering cross sections of OAPB, AOT, and deuterated analogues.

Surfactant	Abbrev.	Formula	SLD (tail) $\cdot 10^{-10}[cm^{-2}]$	MW $[g/mol]$	σ_{coh} [barn]	σ_{inc} [barn]
Oleyl amidopropyl betaine	OAPB	$C_{25}H_{38}O_3N_2$	0.078	424.67	257.8	3853.5
Perdeutero-Oleyl amidopropyl betaine	d-OAPB	$C_{25}H_{38}O_3N_2$	5.936	457.86	384.4	1272.6
Sodium bis-(2-ethylhexyl) sulfosuccinate	AOT	$C_{20}H_{15}D_{33}O_7SNa$	-0.553	444.56	208.3	2971.3
Sodium bis(perdeutero-2-ethylhexyl) sulfosuccinate	d-AOT	$C_{20}H_3D_{34}O_7SNa$	7.696	478.77	338.7	312.1

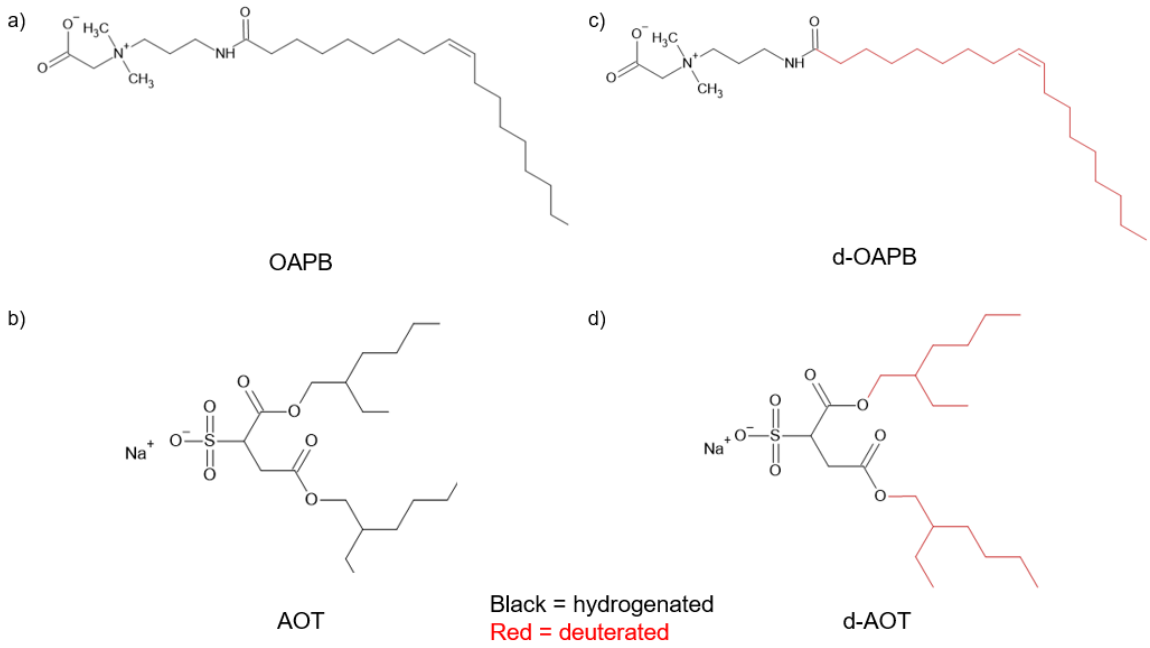

Figure 3.1: Chemical structures of a) OAPB b) AOT c) d-OAPB and d) d-AOT.

All samples were prepared by adding OAPB (or d-OAPB) from an aqueous stock solution to pure AOT (or d-AOT) to obtain the desired concentrations of 40 mM AOT/d-AOT and 20 mM OAPB/d-OAPB. For samples containing salt, NaCl was added from a stock solution to achieve a final concentration of 20 mM.

The samples were then stirred overnight using a magnetic stirrer to achieve full dissolution of the AOT and OAPB. Finally, they were sonicated in a water bath for 5–10 minutes until the solutions became transparent, indicating equilibrium.

3.2. Methods

SANS measurements were performed on the Larmor instrument at the ISIS Neutron and Muon Source (Didcot, UK). The instrument allows a Q range between 0.0035 and 0.7 $Å^{-1}$, with a incident wavelength range of 0.9 to 13.0 Å [30].

Modeling of all scattering data was performed using the software SASView [31], version 6.1.3. For all presented data, symbols represent experimental scattering data and black lines the model fits. The raw scattering data were corrected by subtracting the empty cell, the scattering contribution from D_2O filled cell, and normalized with transmission measurements.

QENS measurements were performed on the IRIS instrument at the ISIS Neutron and Muon Source (Didcot, UK). The instrument allows a Q range between 0.42 and 1.85 $Å^{-1}$, with a resolution of 17.5 μeV [25]. The samples were loaded in an aluminum liquid sample can, with a 1 mm path length and measured at 25 and 37 °C. A PG002 analyzer was used during the experiment.

Modeling of all scattering data was performed using Mantid Workbench [32], version 6.14.0.The raw data were summed and reduced by applying a calibration file obtained from measurements of a cylindrical vanadium standard. The data were subsequently corrected by subtracting the

scattering contribution from the D_2O filled container, scaled by a factor of $(1-\phi)f$, where $f = 0.96$ and ϕ is the volume fraction obtained from the SANS fits.

DLS analyses were performed both on a Malvern DLS Zetasizer, angle 173°, wavelength 628.3 nm and on a Brookhaven NanoBrook Omni, angle 90°, wavelength 640.0 nm.

The samples were loaded into 2.5 mL polymethyl methacrylate (PMMA) cuvettes with a path length of 10 mm. Measurements were performed at 25 and 37°C, with five scans recorded for each sample and a scan duration of 120 s. Prior to each measurement, the samples were left to equilibrate for 180 s at the measurement temperature. The results are shown as an average of the 5 measurements with standard deviation.

Zeta potential measurements were performed by phase-analysis light scattering using a Brookhaven NanoBrook Omni instrument at 25°C. Samples containing 20 mM OAPB and 40 mM AOT, with and without salt, were equilibrated for 1 day before measurement. The Smoluchowski model was used:

$$\mu = \varepsilon_r \varepsilon_0 \eta^{-1} \zeta \tag{3.1}$$

assuming $\kappa a << 1$, where a is the particle radius and κ the inverse of the Debye screening length [33]. In Eq. 3.1, μ is the electrophoretic mobility, ε_r is the solvent dielectric constant, $\varepsilon_0 \approx 8.854 \cdot 10^{-12} \mathrm{C^2 N^{-1} m^{-2}}$ is the vacuum permittivity and η the solvent viscosity [33]. The reported values correspond to the average of 5 consecutivr measurements.

4

Results and discussion

4.1. Self-assembly of OAPB/AOT in water

4.1.1. Salt effects and contrast variation

Oleyl amidopropyl betaine (OAPB) is a zwitterionic surfactants with an 18-carbon unsaturated alkyl tail with a single *cis* double bond between C9 and C10 (Fig. 3.1). In the OAPB/AOT system (20 mM OAPB:40 mM AOT), the SANS data are best described by prolate ellipsoidal micelles ($R_p > R_{eq.}$) at room temperature. The formation of these aggregates is driven primarily by electrostatic interactions between the headgroups of the zwitterionic OAPB and the anionic AOT. Electrostatic attraction between the quaternary ammonium group of OAPB and the sulfonate group of AOT reduces headgroup repulsion, while the hydrophobic interactions between the C18 tail of OAPB and the two branched C6 tails of AOT promote efficient packing in the micelle's core. These interactions favor aggregates with a lower curvature than spherical micelles, resulting in the observed elongated ellipsoidal morphology [34]. In these micelles, the hydrocarbon tails form the hydrophobic core, and the polar headgroups remain exposed in the surrounding aqueous phase.

Upon the addition of 20 mM NaCl, the system undergoes a morphological transition from ellipsoidal micelles to vesicles. This change can be rationalized by considering the effect of salt on the electrostatic interactions: increasing the salt concentration causes charge screening, further reducing electrostatic repulsions between surfactant headgroups. This allows closer molecular packing, decreasing the preferred curvature, and consequently favouring the formation of vesicles over ellipsoidal micelles.

Fig. 4.1 presents the SANS data for the 20 mM OAPB:40 mM AOT system with and without added NaCl. The scattering profile of the salt-free sample is well described by a charged ellipsoid form factor combined with Hayter-MSA structure factor, whereas the sample containing NaCl is best fitted using a core-shell sphere form factor, confirming a salt-induced structural transition.

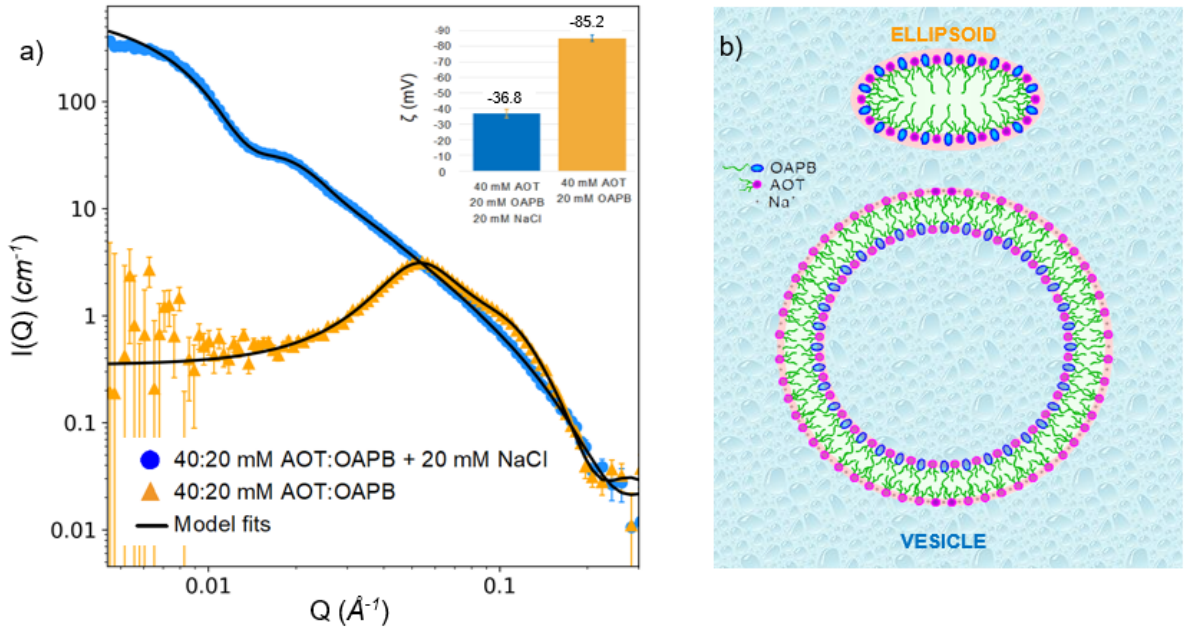

Figure 4.1: a) SANS data and model fits of mixed OAPB and AOT solution (20 mM:40 mM respectively) without (orange) and with (blue) NaCl addition at 25°C. The insert shows zeta potentials (ζ) of 40:20 mM AOT:OAPB with and without 20 mM NaCl at 25°C.. b) Schematic showing an ellipsoidal micelle (top) and vesicle (bottom).

For the vesicles, a hardsphere structure factor was used in the fitting. This model accounts for repulsive interactions between particles approximated as spheres and is appropriate for concentrated systems [35]. Although the addition of 20 mM NaCl screens the electrostatic interactions by acting as a counterion, the vesicles remain charged (Fig. 4.1)[36]. In principle, a more appropriate model would therefore be the Hayter–MSA structure factor, which accounts for electrostatic interactions between charged particles. However, the low Q scattering data do not have enough information, such as showing a charged peak, to determine the parameters of a charged particle model [37]. Furthermore, as shown in Appendix F, fitting the data with only the coreshell form factor results in a poorer description of the low Q region because interparticle interactions are neglected. Although the hardsphere structure factor is not strictly physical for soft matter, it provides a better approximation of the low Q scattering by accounting for short-range interparticle correlations. Consequently, the Hayter–MSA structure factor was not used for further data modelling, and the hardsphere structure factor was adopted instead.

In SANS, it is possible to selectively highlight specific “regions” of a system while minimizing the visibility of others. This is achieved by selectively deuterating certain components, altering the contrast (ΔSLD). By substituting hydrogen with deuterium, one can change the SLD of the molecule. When the molecule SLD is similar to the solvent SLD ($SLD_{D_2O} = 6.36 \cdot 10^{-6}$ Å^{-2}), scattering from the molecule is indistinguishable from the solvent. But, when the SLDs of molecule and solvent are significantly different, then they appear distinctly in the scattering data. This allows not only observing the full morphology of the micelles, but also how AOT and OAPB are independently arranged specifically within the micelle (Fig. 4.2).

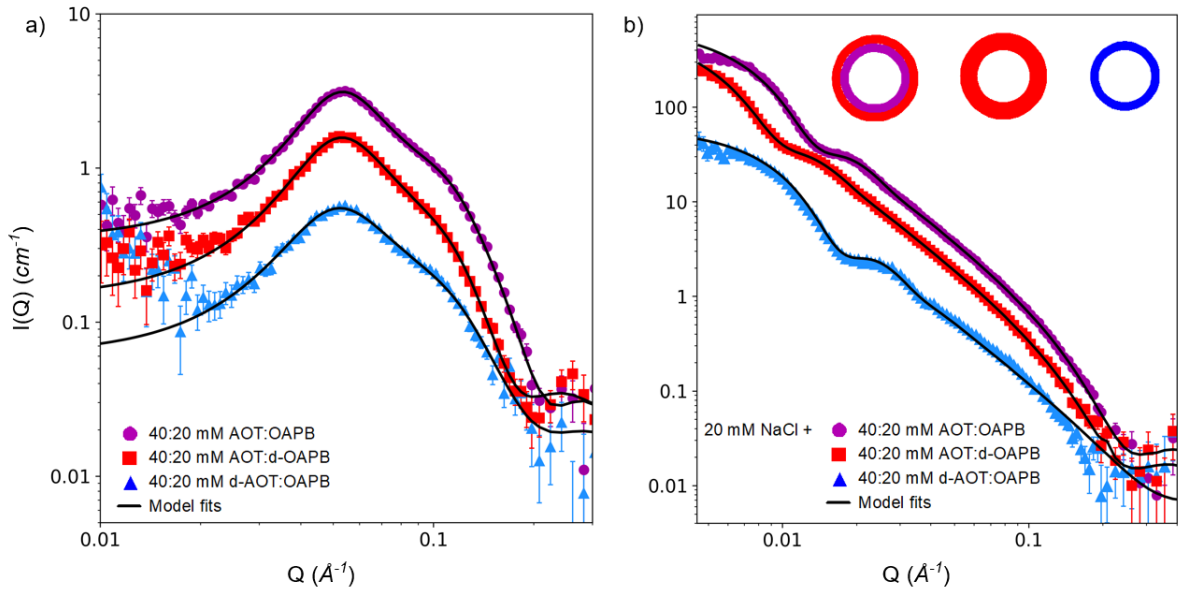

Figure 4.2: a) SANS data and model fits of mixed OAPB and AOT solution (20 mM:40 mM respectively) with non deuterated surfactants (purple), deuterated OAPB (red) and deuterated AOT (blue); b) The corresponding datasets and model fits withd 20mM NaCl. The insert highlights the region of the vesicle bilayer responsible for the SANS signal, corresponding to the non-deuterated component of each sample, since samples were prepared in D_2O.

Table 4.1: Model fitting parameters for 20 mM OAPB and 40 mM AOT with 0 or 20 mM NaCl and with selective deuteration at 25°C.

Composition	Model	$R_{eq.}$ [nm]	R_p [nm]	Charge [e]	ϕ_e [%]	R_v [nm]	PD (R_v) [%]	Thickness$_v$ [nm]	ϕ_v [%]
40 mM AOT 20 mM OAPB	E	1.88 ±0.01	3.26 ±0.04	34.2 ±2.3	2.06 ±0.03	–	–	–	–
40 mM AOT 20 mM d-OAPB	E	2.15 ±0.03	3.30 ±0.09	34.2 ±3.6	2.83 ±0.06	–	–	–	–
40 mM d-AOT 20 mM OAPB	E	1.86 ±0.06	3.33 ±0.18	32.1 ±1.8	2.07 ±0.11	–	–	–	–
40 mM AOT 20 mM OAPB 20 mM NaCl	V	–	–	–	–	19.40 ±0.04	25.0 ±0.1	2.23 ±0.02	9.23 ±0.13
40 mM AOT 20 mM d-OAPB 20 mM NaCl	V	–	–	–	–	27.59 ±0.14	26.4 ±0.3	2.32 ±0.03	10.52 ±0.38
40 mM d-AOT 20 mM OAPB 20 mM NaCl	V	–	–	–	–	15.67 ±0.07	21.9 ±0.3	1.36 ±0.05	7.68 ±0.41

E = Ellipsoid, V = Vesicle

Changing the SLDs (Fig. 4.3) shows that, in the ellipsoidal case, both AOT and OAPB are a part of the same structure, since no noticeable change in size is observed compared to the fully protonated sample, and the overall intensities decrease (Fig. 4.2a). For the vesicle systems, where one might expect an uneven distribution of surfactants within the structure (for example with AOT in the outer leaflet and OAPB in the inner leaflet) a difference in the measured size with deuteration on the order of the bilayer thickness would be observed (Fig. 4.3).

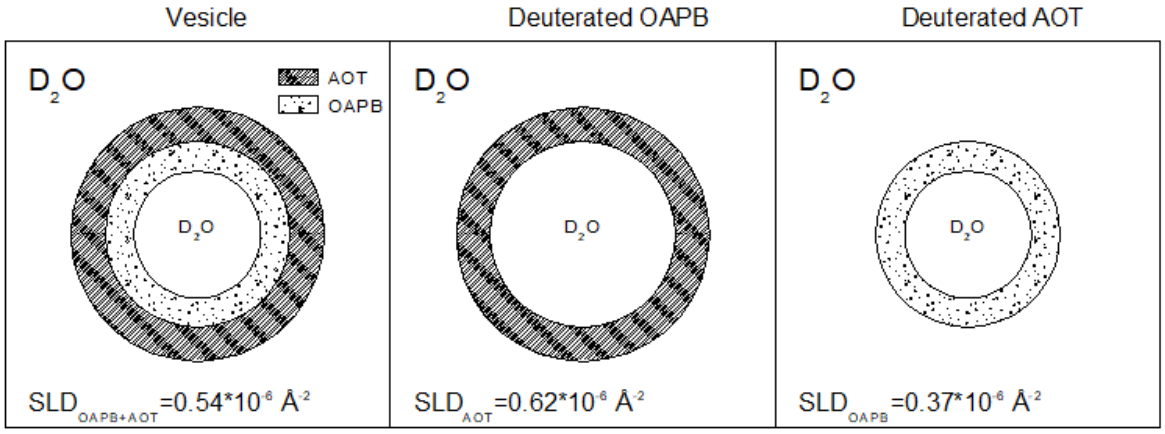

Figure 4.3: Schematic representation of the SLD contrast between AOT and OAPB and their deuterated analogues, highlighting the structural information accessible through SANS measurements. SLDs of single surfactants and combined surfactants are shown.

A difference in size is observed from the fitted data: the fully hydrogenated vesicles exhibit a radius of 19.40±0.06 nm, whereas the vesicular structure in which AOT contributes predominantly to the scattering signal (i.e. deuterated OAPB) has a radius of 27.59±0.14 nm. In contrast, the structure for which the scattering arises mainly from OAPB (*i.e.*, deuterated AOT) exhibits a radius of 15.67±0.07 nm. The differences in radius between samples are considerably larger than the bilayer thickness. Furthermore, as shown in Table 4.1, the fitted lognormal polydispersities of the vesicle systems are $(25.0 \pm 0.1\%)$, $(26.4 \pm 0.3\%)$, and $(21.9 \pm 0.3\%)$ for the fully protonated, deuterated OAPB, and deuterated AOT samples, respectively. These values indicate that all three systems exhibit relatively broad size distributions. Consequently, the fitted radii should be interpreted as the mean values of a distribution of vesicle sizes rather than as the size of a single, monodisperse population. Therefore, the size difference probed with contrast variation cannot be used to draw conclusions regarding the arrangement of the individual surfactants within the vesicle.

Although the vesicle size does not provide any definitive conclusions, an important observation emerges from the analysis of the bilayer thickness. Model fits for both the fully hydrogenated sample and the sample with deuterated OAPB yield a bilayer thickness of respectively 2.23±0.02 and 2.32±0.03 nm. In contrast, the sample in which the scattering signal arises primarily from OAPB exhibits a thickness of 1.36±0.05 nm. This result suggests that AOT is present in both the inner and outer leaflets of the vesicle membrane. In contrast, OAPB appears to be mostly located in one leaflet, within the instrument detection limit, since the thickness measured for that sample is smaller than that of the fully hydrogenated vesicles. Furthermore, given the size difference between this sample ($R_v = 15.7$ nm) and the fully protonated one ($R_v = 19.4$ nm), it can be speculated that OAPB is predominantly located in the inner layer, as evidenced by the smaller vesicle size, bearing in mind the points discussed above. This interpretation is consistent with the hypothesis proposed in a previous study [7].

A bilayer thickness of 1.4 nm may appear small when considering the length of the OAPB hydrocarbon chain (from Tanford $l_c = 2.43$ nm) . However, it should be kept in mind that OAPB molecules possess a kink in their carbon tail and undergo confined motions, as discussed in Section 4.2.4. Consequently, the surfactant molecules are neither fully extended nor rigid, but instead adopt a more fluid and flexible conformation, which can account for the observed thickness.

4.1.2. Vesicle to ellipsoid transition

Changes in temperature have an impact on the self-assembly of AOT and OAPB. It was found, for a system containing 20 mM of NaCl and an OAPB:AOT ratio of 20:40 mM, that increasing the temperature from 25 to 50°C leads to a transition from vesicles to ellipsoidal micelles (Fig. 4.4). The increase in thermal energy enhances the mobility of the surfactants, altering the balance of interactions (discussed in depth in Section 4.2.3). This enhanced fluidity and the weakening of these interactions may be responsible for the transition toward structures with higher curvature.

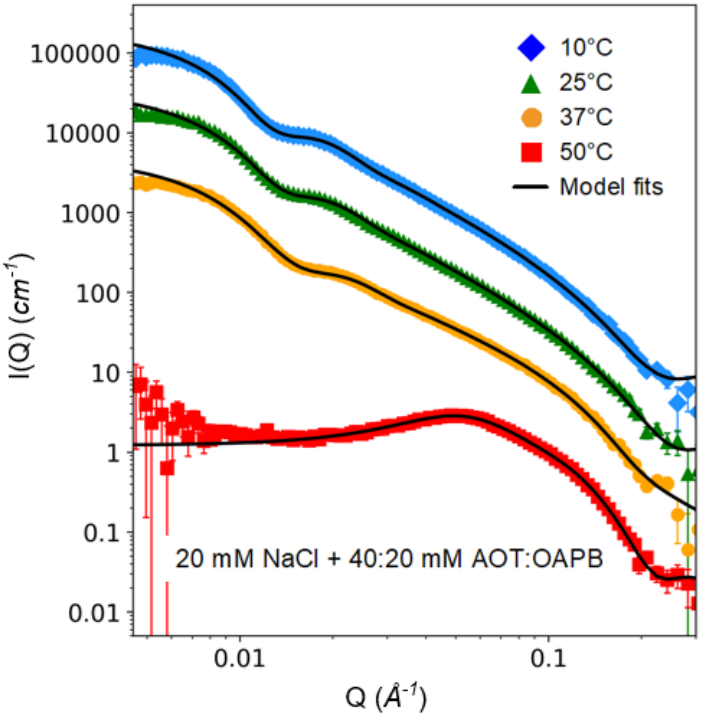

Figure 4.4: SANS data and model fits of OAPB and AOT solution (20 mM:40 mM respectively) with 20 mM NaCl at different temperatures. Data have been offset for readability.

Table 4.2: SANS model parameters for 20 mM OAPB and 40 mM AOT with 20 mM NaCl at different temperatures.

T [°C]	Model	S(Q)	$R_{eq.}$ [nm]	R_p [nm]	Charge [e]	ϕ_e [%]	R_v [nm]	PD (R_v) [%]	Thickness$_v$ [nm]	ϕ_v [%]
10	V	HS	–	–	–	–	20.65 ±0.04	23.8 ±0.1	2.40 ±0.02	8.85 ±0.15
25	V	HS	–	–	–	–	19.40 ±0.04	25.0 ±0.1	2.23 ±0.02	9.23 ±0.13
37	E+V	–	2.04 ±0.03	22.08 ±7.22	–	0.84 0.03	17.03 ±0.14	24.6 ±0.5	1.88 ±0.11	5.50 ±0.58
50	E	HP	1.82 ±0.01	4.06 ±0.06	25.1 ±0.6	1.81 ±0.06	–	–	–	–

HS = Hardsphere, HP = Hayter-Penfold

The fitted ellipsoidal micelles that form at 50°C exhibit a charge peak around $Q = 0.07$ Å^{-1}, despite the presence of salt in the system. It is hypothesized that, at 50 °C, the salt screening effect between the headgroups, which effectively decreases the headgroup area and therefore favors structures with lower curvature, is no longer sufficient to counterbalance the increased thermal motion of the surfactants. As a result, the surfactant molecules are unable to pack as closely, leading to an increase in the preferred curvature. Consequently, the vesicles collapse into smaller ellipsoidal structures.

This phenomenon appears to start occurring, 37°C. At high Q values, the data exhibit a steeper decay towards high Q, comparable to that observed for the ellipsoid model. This behavior prevents a completely accurate fit when only a core-shell model is employed. Therefore, in order to obtain both an adequate fit and a physically meaningful description of the system, two different models were then combined: a core-shell sphere model and an ellipsoid model (Fig. 4.5).

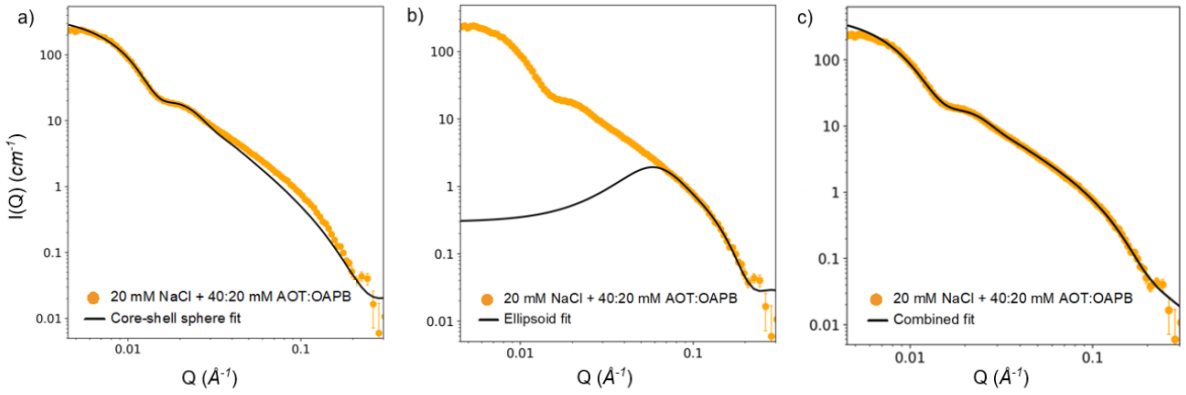

Figure 4.5: SANS data of mixed OAPB and AOT solution (20 mM:40 mM respectively) with 20 mM NaCl at 37°C. a) A Core-shell sphere model is used to describe the data at low Q; b) Ellipsoid model is used to describe the data at high Q; c) Core-shell model sphere was summed to the ellipsoid model to describe the data.

The results of this modeling approach, however, should be treated with caution. The reason is that the scattering from the vesicles at low Q overlaps with the scattering originating from the ellipsoidal micelles, resulting in the coexistence of both structures. Due to this overlap, the results for the parameters yield a polar radius approximately ten times larger than the equatorial radius, corresponding to a highly elongated ellipsoid, which is effectively equivalent to a cylinder or rod-like micelle.

To confirm the presence of ellipsoids, and obtain satisfactory output results, data were first fitted with a core-shell model representing the vesicles. The fitted vesicle contribution was then subtracted from the original scattering data, and the resulting residual scattering was subsequently fitted. This analysis revealed features consistent with the presence of ellipsoidal micelles (Fig. 4.6).

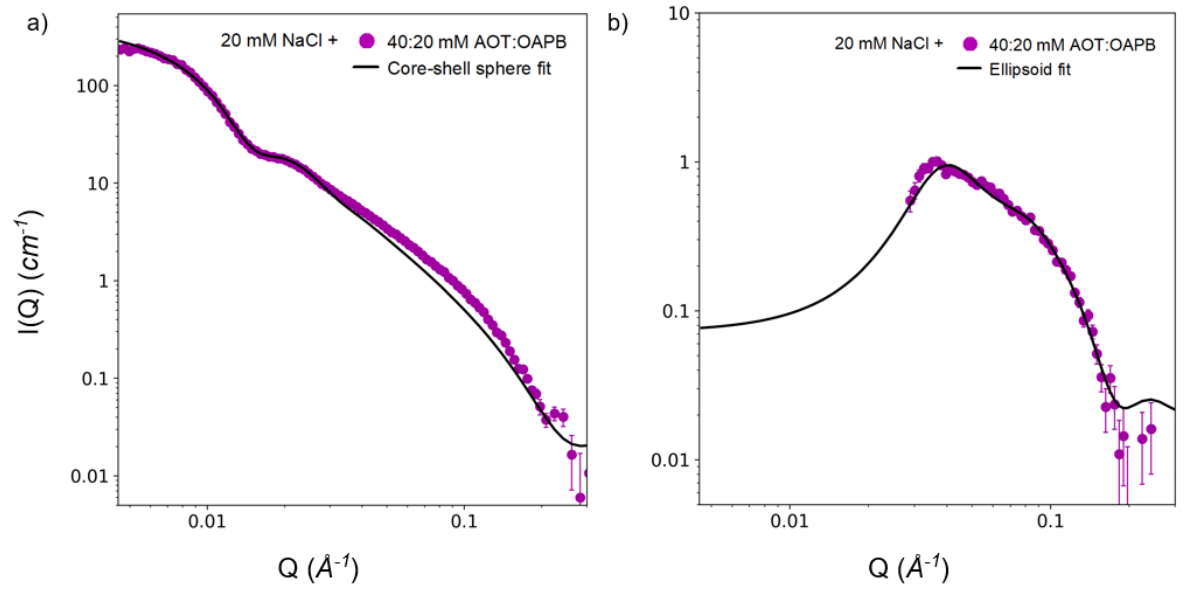

Figure 4.6: a) SANS data and core-shell sphere model fit of mixed OAPB and AOT solution (20 mM:40 mM respectively) and 20mM NaCl at 37°C b) Data obtained from the subtraction of the core-shell sphere model from the original data; ellipsoidal model fit.

Table 4.3: SANS model parameters for 20 mM OAPB and 40 mM AOT with 20 mM NaCl at 37 °C for the ellipsoid model after data subtraction (Fig. 4.6b).

Composition	Model	$R_{eq.}$ [nm]	R_p [nm]	Charge [e]	ϕ_e [%]
40 mM AOT 20 mM OAPB 20 mM NaCl	E	2.20 ±0.07	2.88 ±0.19	25.96 2.29	1.02 0.04

As similarly reported by [7], Fig. 4.6 shows that increasing temperature from 25 to 37°C induces transition from vesicular aggregates to ellipsoidal micelles. As discussed in Section 4.2.3, the transition is attributed to the increased diffusion of individual molecules resulting from the higher thermal energy, which ultimately increases the membrane fluidity. This enhanced mobility allows the surfactants to adopt structures higher curvature. In contrast to the observations of [7], where a complete vesicle to ellipsoid transition occurred, the transition at 37 °C is incomplete at the concentration investigated in this work. It is proposed that the higher surfactant concentration increases the steric hindrance between aggregates, requiring additional thermal energy to overcome this constraint. Consequently, the complete transition is only observed at 50 °C.

Finally, it is possible to determine whether the ellipsoidal structures arise from the mixed surfactant system or from the contribution of a single surfactant. Individually, OAPB and AOT are known to form wormlike micelles [5] and ellipsoidal micelles [6], respectively. Therefore, analysis of the deuterated sample can help determine whether the ellipsoidal micelles observed in Fig. 4.5 arise from the segregation of one surfactant from the mixed aggregates or instead contain both surfactants.

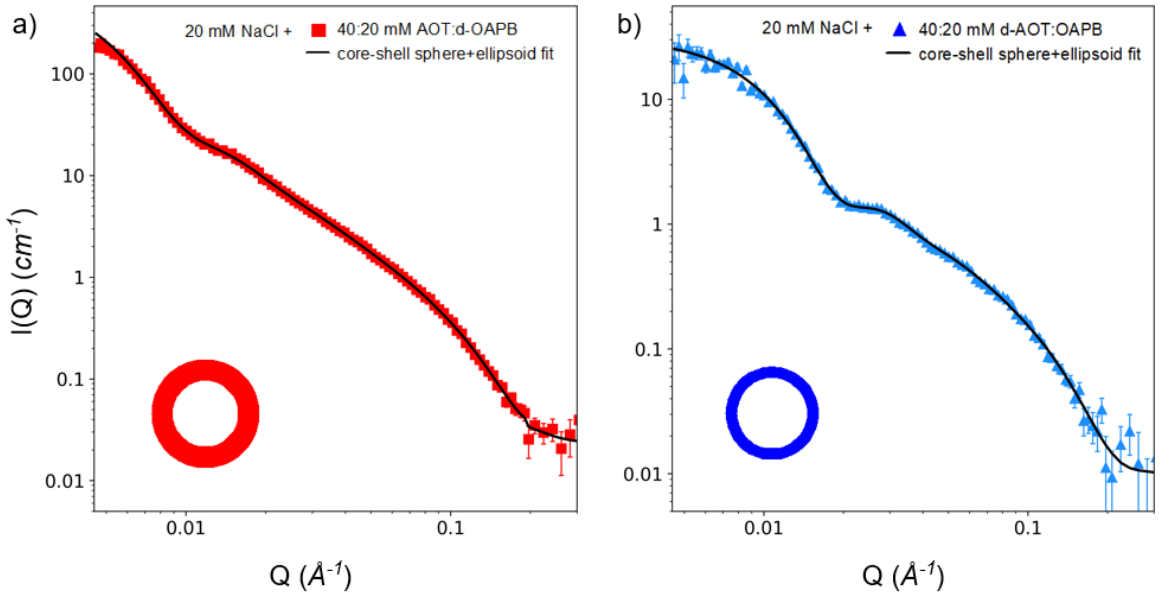

Figure 4.7: SANS data and model fits of mixed OAPB and AOT solution (20 mM:40 mM respectively) and 20mM NaCl with a) deuterated OAPB (red) and b) deuterated AOT (blue) at 37°C, with a schematic representation of the observed structure.

In Fig. 4.7, a combined core-shell/ellipsoid model was used to fit the data. Both models provide a good fit to the data. However, the high Q region does not provide sufficient information to accurately determine the parameters of the ellipsoidal micelles coexisting with the vesicles, as the fitted parameter are not well constrained (Table B.1). Nevertheless, these results indicate that OAPB and AOT remain mixed throughout the system. Consequently, the second micellar population is unlikely to arise from the segregation of one surfactant species, highlighting the importance of surfactant mixing in stabilizing the coexistence of multiple aggregate morphologies.

4.1.3. Debye radius and charge ellipsoid

For samples with no salt addition, an increase in temperature does not cause transitions between different micellar structures (Fig. 4.8). The systems remain ellipsoidal, exhibiting only a slight decrease in size.

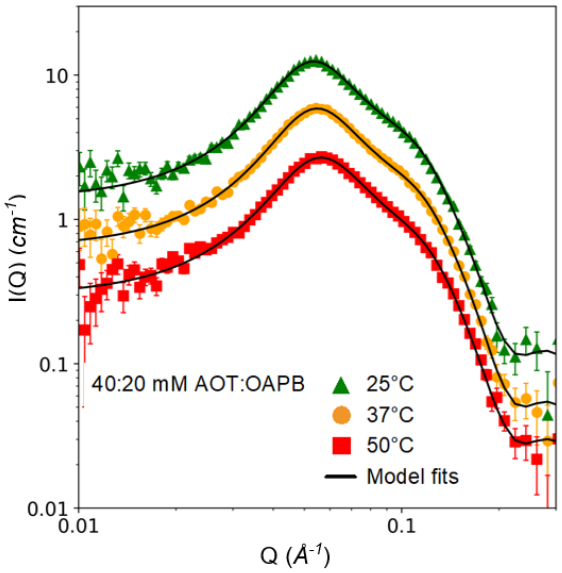

Figure 4.8: SANS data and model fits of mixed OAPB and AOT solution (20 mM:40 mM respectively) at different temperatures without salt addition. Data are offset for readability. Data at 10°C are shown in Appendix E, since at this temperature the systems behaves significantly differently.

Table 4.4: SANS model parameters for 20 mM OAPB and 40 mM AOT at different temperatures.

Temperature [°C]	Model	$R_{eq.}$ [nm]	R_p [nm]	Charge [e]	ϕ_e [%]
25	E	1.88 ±0.01	3.26 ±0.04	34.2 ±2.3	2.06 ±0.03
37	E	1.86 ±0.01	3.16 ±0.05	32.4 ±2.1	2.10 ±0.03
50	E	1.84 ±0.02	3.08 ±0.05	27.2 ±1.6	2.20 ±0.04

In a previous study [7], it was found that in a salt-free solution containing 20 mM AOT and 10 mM OAPB, the surfactants aggregate at 25°C to form a mixture of vesicles and ellipsoids, while only ellipsoidal micelles are observed upon heating to 37°C. Therefore, an additional excluded volume effect (particles cannot occupy the same space) arising from electrostatic interactions must be present. In more concentrated systems, these interactions may hinder the formation of larger structures, such as vesicles, not only because of the larger number of aggregates and the resulting stronger excluded volume effects, but also because electrostatic interactions, characterized by the Debye length, can lead to overlap between neighboring aggregates. Such overlap would increase the free energy of the system, making the formation of vesicular structures less favorable.

To investigate these interactions, a dilution series ranging from 40:20 mM to 20:10 mM AOT:OAPB was prepared and measured using SANS at both 25°C and 37°C in order to determine the dependence of the Debye radius on number of micelles (Fig. 4.9).

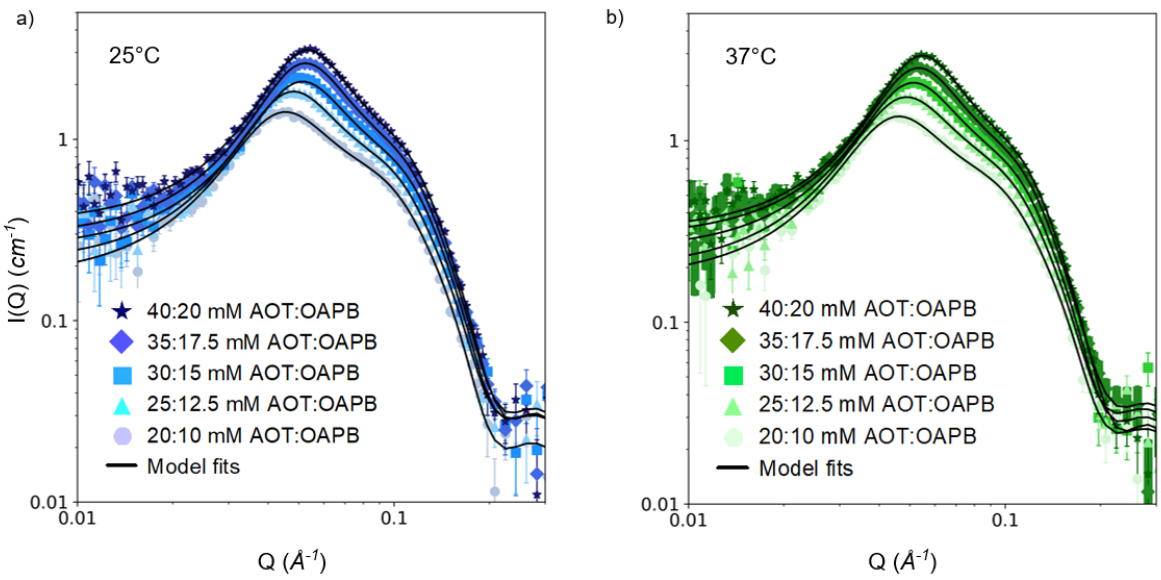

Figure 4.9: SANS data and model fits of mixed OAPB and AOT solution at fixed surfactant ratio (2:1 AOT:OAPB) at a) 25°C b) 37°C.

The dilution series showed a decrease in the Debye length with increasing surfactant concentration in solution (Fig. 4.10). The Debye length (κ^{-1}) can be defined as the distance from a charged surface at which the electrostatic potential has decayed to $1/e$, or 36.7%, of its value at the surface [38]. It can be calculated from the ionic strength of the electrolyte in solution, I, which was obtained from the SANS fits (Appendix C and Fig. 4.9). Debye lengths across the dilution series were calculated using Eq. 4.1 [38].

$$\kappa^{-1} = \sqrt{\frac{\varepsilon_0 \varepsilon_r k_B T}{2 N_A q_e^2 I}} \tag{4.1}$$

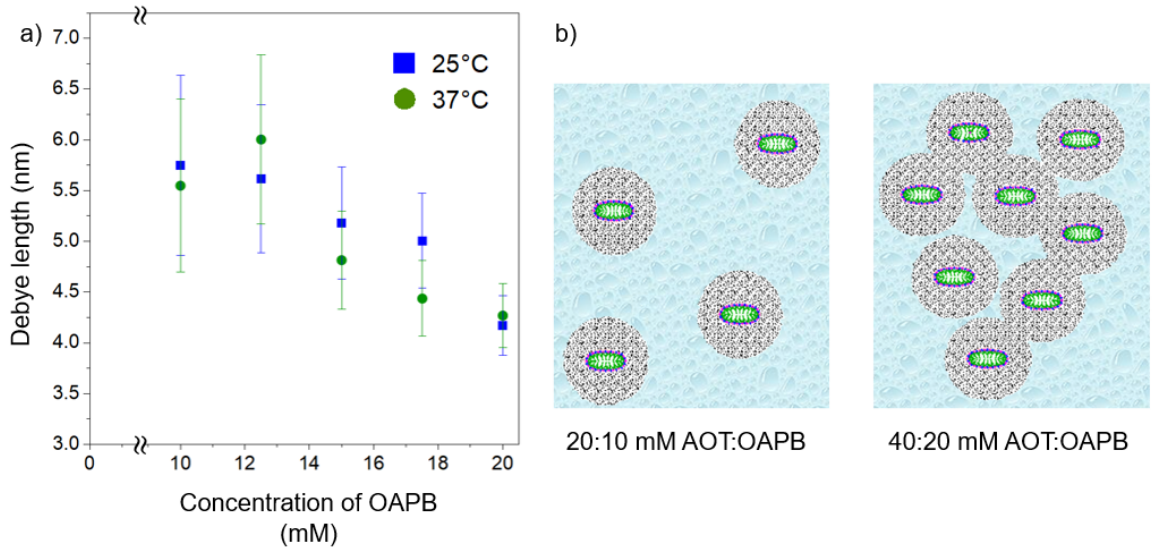

Figure 4.10: a) Debye length dependence with concentration for AOT:OAPB 2:1 ratio at 25°C (blue) and 37°C (green); b) Schematic representation of repulsions due to excluded volume effects end electrostatic interactions (Debye length in grey) for 20:10 mM AOT:OAPB snd 40:20 mM AOT:OAPB ellipsoidal micelles in water.

Fig. 4.10 shows that the Debye length decreases with increasing surfactant concentration, indicating stronger electrostatic screening. Nevertheless, higher concentrations lead to a larger number density of aggregates and stronger excluded volume effects. Since the dimensions of the ellipsoidal micelles are comparable to the Debye length, interactions between neighboring micelles remain significant and may hinder the formation of larger vesicular structures, favoring instead the formation of smaller ellipsoidal aggregates.

Increasing the temperature to 37°C does not significantly change the Debye length of the ellipsoidal micelles (Fig. 4.10), with the values remaining comparable, within experimental uncertainty, to those obtained at 25°C. According to Eq. 4.1, the Debye length depends on both temperature and the relative dielectric constant of the solvent. While an increase in temperature increases the Debye length, the relative dielectric constant of water decreases with increasing temperature [39]. As a result, Debye length between the two temperatures are comparable in the error margin.

In these measurements, the 20:10 mM (AOT:OAPB) system did not show the coexistence of vesicles and ellipsoids as reported in [7]. This discrepancy could be attributed to differences in sample preparation methods. In the reported study, the sample was prepared directly at the desired concentration, allowing the surfactants to aggregate and organize freely. In contrast, for this work the sample was prepared by gradually diluting the 40:20 mM AOT:OAPB solution, meaning that solvent was added to a system in which ellipsoidal structures were already stable and formed. Therefore, to determine the transition concentration at which electrostatic repulsion and excluded volume effects prevent the formation of vesicles due to their bigger size, fresh samples should be prepared directly at each concentration and analyzed, rather than obtained by diluting a higher concentration solution.

4.2. Dynamics of OAPB/AOT system

4.2.1. Data processing and modeling approach for QENS spectra

QENS data from a 20 mM OAPB and 40 mM AOT sample, measured at 25 and 37°C using IRIS ($\Delta E = 17.5\ \mu eV$) [40], show quasi-elastic broadening beyond the instrumental resolution, obtained by measuring a cylindrical vanadium standard (Fig. 4.11), indicating the presence of dynamic processes in the system.

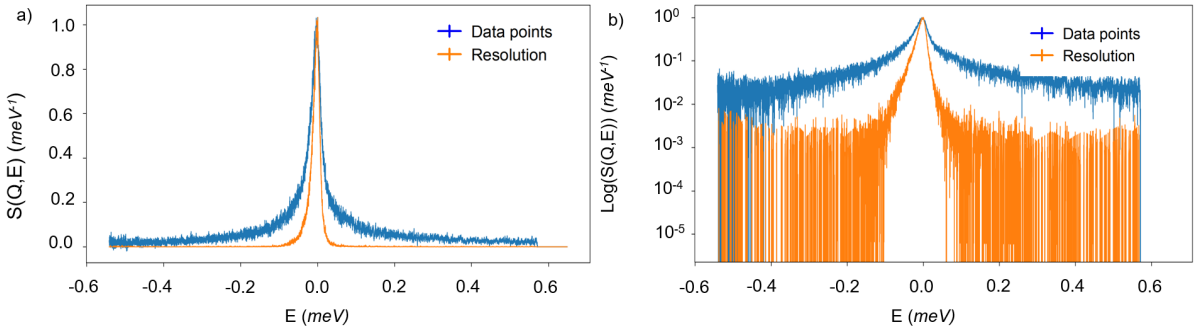

Figure 4.11: Quasi-elastic broadening beyond the instrumental resolution for AOT/OAPB vesicles (40:20 mM) at $Q = 0.94$ Å^{-1}: a) linear scale, b) logarithmic scale for better visualization of the spectrum broadening.

The data were fitted using a model consisting of the convolution of two Lorentzian functions, both centered at ($E = 0$ meV) (Fig. 4.12). One Lorentzian is relatively narrow, while the other is considerably broader. The success of this model in describing the experimental spectra suggests the presence of at least two distinct dynamical processes. The narrower Lorentzian is attributed to the slower motion of the aggregates, whereas the broader Lorentzian is associated with the faster localized motion of the individual surfactant molecules. The dynamic structure factor used to fit QENS spectra is given in Eq. 4.2 [41]:

$$S(Q,\omega) = [EISF \cdot L_1 + (1 - EISF) \cdot L_2] \otimes Res \tag{4.2}$$

Here, the Elastic Incoherent Structure Factor (EISF) is defined as the ratio of the elastic scattering intensity to the total neutron scattering intensity [10]. It weights the contributions of the first (L_1) and second (L_2) Lorentzians, which are convoluted with the instrumental resolution (i.e. the measured signal is a contribution of both the true signal and the instrument response time, which“smears” the real signal).

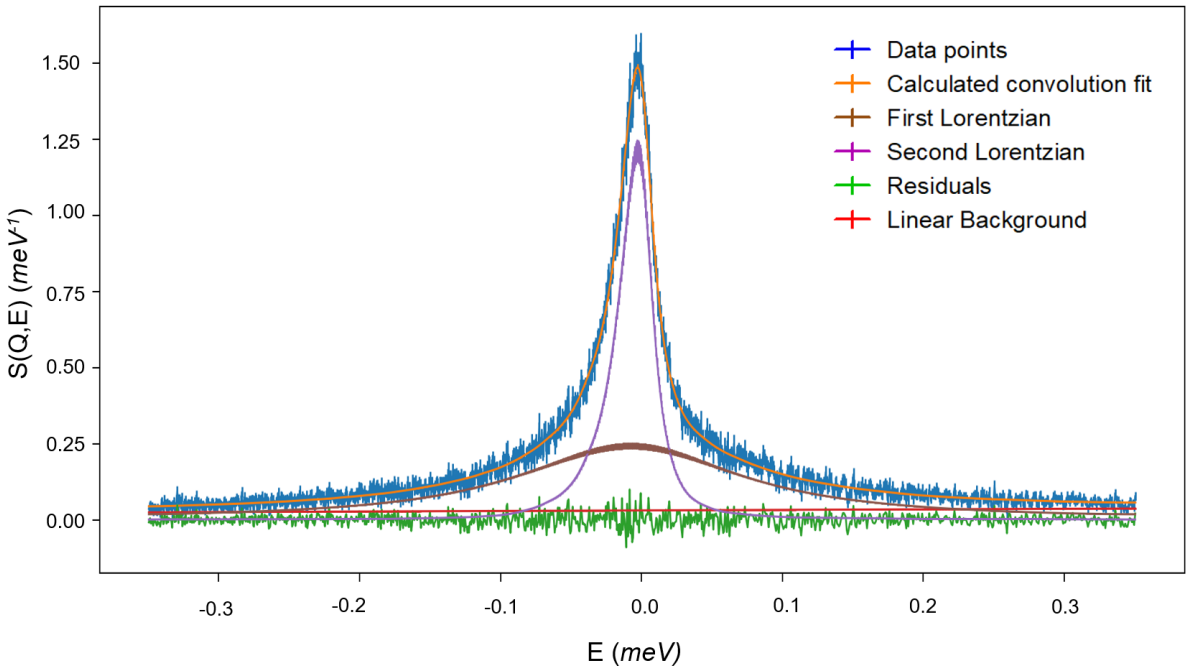

Figure 4.12: Typical fitted QENS spectrum for AOT/OAPB vesicles (40:20 mM) at $Q = 0.94$ Å^{-1}. The residuals (green) indicate good fit quality.

To better understand the dynamic processes in the system, as well as the influence of temperature and salt addition, the FWHMs of the two Lorentzians and the EISF were analyzed.

4.2.2. Vesicle diffusion in solution

To investigate the contribution of each surfactant to the system dynamics, selective deuteration was applied to the surfactant tails. By substituting these hydrogen atoms with deuterium, it is possible to reduce the incoherent scattering signal from that surfactant, since $\sigma^D_{\text{inc}} = 2.050$ barn and $\sigma^H_{\text{inc}} = 80.27$ barn [20]. Consequently, the measured signal originates predominantly from the second (hydrogenated) surfactant [41], and was carried out alternately for both AOT and OAPB (as with the SANS measurements in Section 4.1). Fig. 4.13 shows the linear dependence of the FWHM on Q^2 for vesicles with 40:20 mM AOT:OAPB at 25°C, in the presence of 20 mM NaCl as a counterion in D_2O.

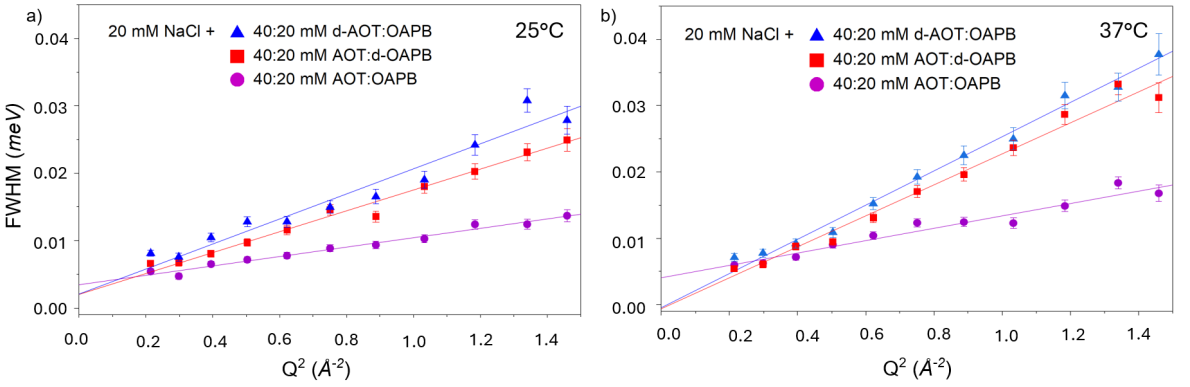

Figure 4.13: Variation of the FWHM of the first Lorentzian as a function of Q^2 at the specified deuteration conditions, measured at a) 25°C and b) 37°C.

The linear dependence of the FWHM on Q^2 is characteristic of Fickian diffusion, as described by Eq. 4.3 [42]:

$$\text{FWHM} = \frac{1}{2} D_{eff} Q^2 \tag{4.3}$$

From the slope of this linear relationship, the diffusion coefficient (D_{eff}) can be extracted. The results are summarized in Table 4.5.

Table 4.5: Determined diffusion coefficients of vesicles in aqueous solution with different chemical deuterations at 25°C and 37°C.

Composition	Isotope	T [°C]	$D_{eff} \cdot 10^{10}$ [m^2/s]	Error $\cdot 10^{10}$ [m^2/s]
40 mM d-AOT 20 mM OAPB 20 mM NaCl	D H -	25	1.41	0.13
		37	1.96	0.07
40 mM AOT 20 mM d-OAPB 20 mM NaCl	H D -	25	1.18	0.05
		37	1.77	0.10
40 mM AOT 20 mM OAPB 20 mM NaCl	H H -	25	0.53	0.03
		37	0.71	0.06

These determined diffusion coefficients contain both Brownian diffusion behaviour and rotational diffusion. In the case of this system, it is not possible to distinguish the two dynamic behaviors probed by QENS (Appendix G). Brownian diffusion of vesicle in solution follows the Stokes-Einstein equation [29]:

$$D_{eff} = \frac{k_B T}{6\pi\eta R_h} \tag{4.4}$$

where k_B is the Boltzmann's constant, η is the solvent viscosity and R_h the hydrodynamic radius [29]. According to Eq. 4.4, an increase in temperature leads to faster diffusion. Vesicle diffusion is not a thermally activated process, in the sense that vesicles have to overcome an activation energy barrier; instead, increasing the temperature leads to more frequent collisions between particles and solvent molecules. These collisions generate momentum transfer, which results in Brownian diffusion.

A difference in the extrapolated diffusion coefficient can be observed between the deuterated samples and the fully protonated sample, with the former diffusing approximately twice as fast as the latter (Table 4.5). For deuterated samples, the scattering contribution from one of the two surfactants is weaker, however, this should not influence the diffusion of the entire vesicle, which moves as a single entity. Therefore, for vesicles of comparable size at the same temperature (according to Eq. 4.4), the diffusion coefficients should be approximately the same regardless of whether the sample constituents are deuterated or protonated. To investigate this discrepancy, which is observed at both 25 and 37°C, diffusion coefficients were additionally determined using Dynamic Light Scattering (DLS, Fig. 4.14).

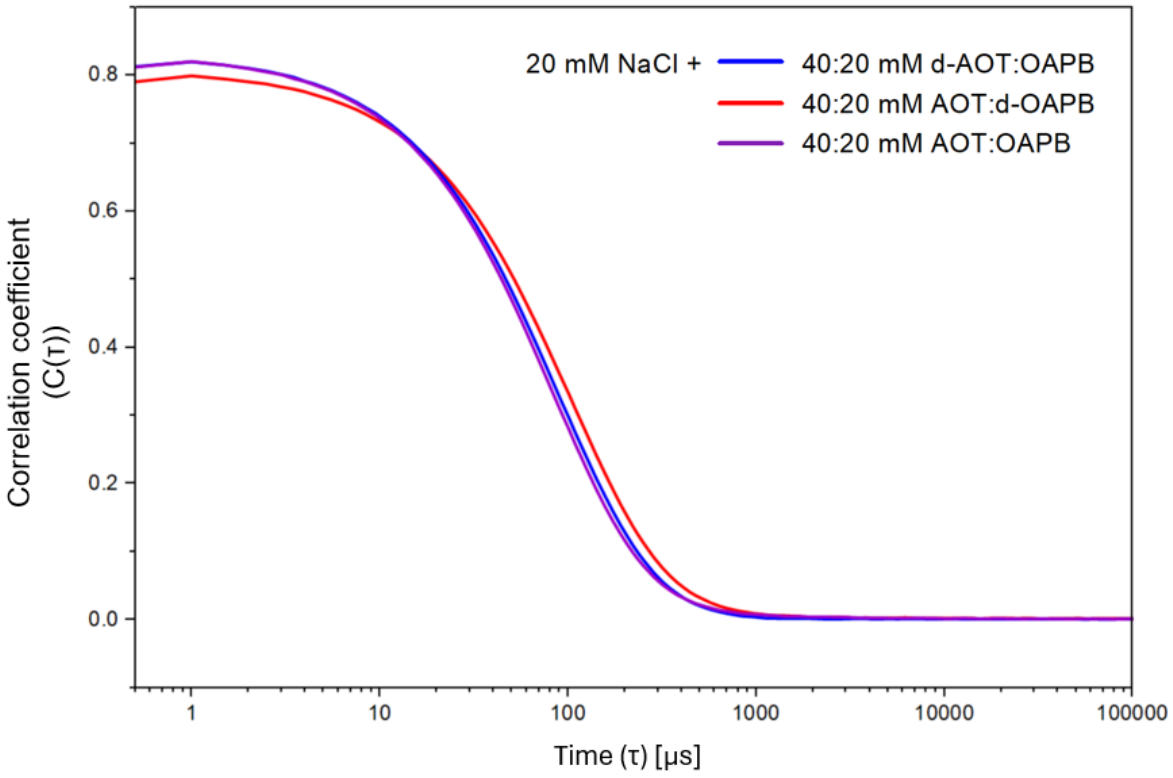

Figure 4.14: Dynamic Light Scattering correlation functions for the three sample variations at 25°C.

Given that these measurements were to identify diffusion differences between the deuterated and protonated systems, rather than to obtain highly accurate diffusion coefficients, the data were fitted using the approximation of monodisperse, spherical particles undergoing Brownian diffusion [29]. Under this assumption, the intensity autocorrelation function decays exponentially with the delay time, τ, as described by Eq. 2.12 [29].

The DLS measurements reported the following diffusion coefficients, shown in Table 4.6:

Table 4.6: Diffusion coefficients for the three sample variations obtained from Dynamic Light Scattering at 25°C.

Composition	Isotope	T [°C]	$D_{eff} \cdot 10^{11}$ [m^2/s]	Error $\cdot 10^{11}$ [m^2/s]
40 mM d-AOT 20 mM OAPB 20 mM NaCl	D H -	25	1.42	0.01
40 mM AOT 20 mM d-OAPB 20 mM NaCl	H D -	25	1.22	0.02
40 mM AOT 20 mM OAPB 20 mM NaCl	H H -	25	1.51	0.03

The diffusion coefficients obtained are approximately one order of magnitude smaller than those determined by fitting the FWHM of the first Lorentzian. It should be noted that the timescales probed by QENS are on the order of hundreds of picoseconds, which are too short for entire vesicles to undergo diffusion, and also to distinguish between Brownian and rotational diffusion [10]. Instead, the QENS signal arises predominantly from the incoherent scattering of hydrogen atoms, whose motions occur on these faster timescales [10]. The hydrogen atoms undergo localized motions and vibrations, and the extracted diffusion coefficients therefore are related to the physical interpretation of the hydrogen dynamics observed from the experiment. Consequently, the diffusion coefficients obtained from QENS differ from those measured by DLS, which probes only the diffusion of entire vesicles over much longer timescales. As a result, the apparent diffusion coefficients derived from QENS are larger than those measured by DLS.

That said, the DLS measurements, even though yield different values for diffusion coefficients do not show the same discrepancy between deuterated and protonated sample as observed from the $FWHM$. Furthermore, the sample containing deuterated OAPB, which exhibited the slowest diffusion coefficient behaved consistently with the SANS measurements (the DLS measurements were performed prior to the SANS experiments), yielding the largest vesicle radius. This consistency raises the possibility that deuteration influences the self-assembly of the mixed surfactant system. However, to the best of my knowledge, no literature has reported differences in the aggregation behaviour of the hydrogenated and deuterated surfactants that would explain the observed trend. This inconsistency therefore requires further investigation.

The first possible explanation is that the protonated sample was fitted inaccurately, as the obtained value of D_{eff} is inconsistent with what would be expected. To test this hypothesis, additional fits were performed by imposing upper and lower boundaries on both the amplitude and the FWHM (the fitting boundaries for the hydrogenated sample were set to the values obtained for the deuterated sample, with a tolerance of four times the uncertainties). The corresponding results are presented in Appendix I. These constrained fits hit the imposed parameter boundaries and produced structured residuals between the experimental data and the fitted model. This indicates that the constrained fits do not adequately describe the data, thereby ruling out an incorrect fit as the origin of the observed discrepancy.

Another hypothesis to explain the observed difference in behavior is based on the isotopic effect resulting from the substitution of hydrogen with deuterium in the surfactant tails. Deuterium has a greater mass than hydrogen ($m_D = 2.014$u, $m_H = 1.008$u [43]), and, consequently, a lower zero-point vibrational energy [44]. The zero-point vibrational energy corresponds to the lowest energy level at which atoms still exhibit vibrational motion [45]. This implies that atoms are never completely at rest, even at their minimum energy state, but continue to vibrate (Fig. 4.15).

The zero-point vibrational energy is inversely proportional to the reduced mass (μ) of the vibrating system (Eq. 4.5), and differences in vibrational energy are therefore expected for light isotopes [46], such as hydrogen and deuterium.

$$\frac{1}{\mu} = \frac{1}{m_A} + \frac{1}{m_H} \text{ or } \frac{1}{m_D} \tag{4.5}$$

with m_A mass of the other atom [46].

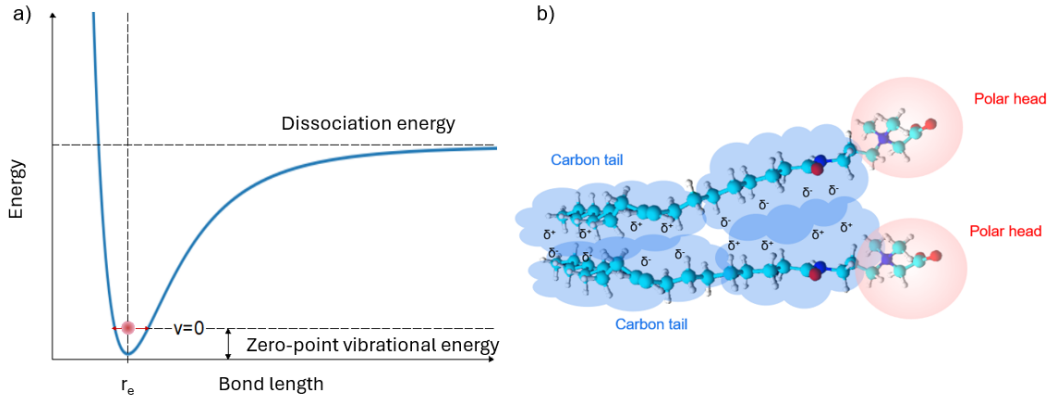

Figure 4.15: a) Schematic representation of an atom (red) vibrating at the zero-point potential, where r_e is the equilibrium distance; b) Schematic representation of interaction between carbon tails (blue) in surfactants due to instantaneous dipoles.

Therefore, replacing hydrogen with deuterium decreases the zero-point vibrational energy of the bond, leading to a shorter bond length for C-D and a higher bond dissociation energy than that of the C-H bond [44]. This difference in vibrational energy and bond length results in a slightly larger dipole moment for C-D bonds, as the electron density is more confined as a result of its shorter bond length [47],[48]. On a larger scale, fluctuations in the electron cloud surrounding these atoms are responsible for the intermolecular interactions between the surfactant tails, namely the London dispersion forces, illustrated in Fig. 4.15.

This interaction is a driving force of self-assembly. In the case of deuterated surfactants, the slightly higher dipole moment of the C–D bonds at large scales likely leads to stronger attraction between surfactants within the vesicle. This may be responsible for a decrease in membrane fluidity. Notably, if the dynamics of the membrane (which are not visible by DLS) occur on the same timescale as vesicle diffusion, then QENS is no longer capable of distinguishing between the two different dynamic processes, leading to a different apparent D_{eff}, as a result of cumulative effect. Nevertheless, to the best of my knowledge, quantitative differences in the dipole moments of C-D and C-H bonds have not been reported in the literature. The available studies that discuss this possibility reach similar qualitative conclusions regarding the effect of deuteration on dipole moments but do not provide quantitative values for the dipole moment differences. Instead, the reported dipole moments generally correspond to bonds involving hydrogen or deuterium with atoms other than carbon [48]. However, some studies discuss the slightly higher stability of hydrogen bonding upon deuterium substitution, basing this discussion on differences in zero-point vibrational energy [49].

4.2.3. Lateral diffusion of surfactants within the membrane bilayer

The second Lorentzian obtained from the QENS analysis represents the combined contribution of two dynamic processes present in the system [27]. In the present case, these correspond to the global diffusion of the vesicles (discussed in the previous section) and the local motion of individual surfactant molecules within the micelle structure. It can therefore be expressed as Eq. 4.6

$$L_2(\omega) = \frac{FWHM_1 + FWHM_2}{(FWHM_1 + FWHM_2)^2 + (\hbar\omega)^2}, \tag{4.6}$$

where $FWHM_1 + FWHM_2$ is the total linewidth obtained from the QENS fit, with $FWHM_1$ and $FWHM_2$ corresponding to the first and second dynamic processes, respectively. Since $FWHM_1$ is already known from the narrow Lorentzian, the contribution of the second dynamic process can be isolated by subtracting $FWHM_1$ from the fitted quantity $FWHM_1 + FWHM_2$ [50]. The resulting $FWHM_2$ exhibits a linear dependence on Q^2 (Fig. 4.16), again following Eq. 4.3, indicating that this process is also diffusive.

Because the second Lorentzian is broader, it corresponds to a faster dynamic process occurring on shorter timescales. Although both Lorentzians display Brownian diffusion, they describe motions on different length and time scales. The narrow Lorentzian captures the translational diffusion of the vesicles as whole objects, whereas the broader Lorentzian reflects the diffusion of smaller entities within the system. In the AOT/OAPB vesicle system, this faster process is attributed to the lateral diffusion of individual surfactant molecules within the vesicle bilayer. This is possible because the membrane is not rigid but fluid. While the surfactants do pack sufficiently closely to form compact structures such as vesicles, several factors prevent tight or immobile packing: the asymmetry between the inner and outer leaflets, the presence of a double bond at the C9 position in OAPB, and the branched double-tail structure of AOT. As a result, free volume exists between the surfactant molecules, allowing them to move laterally within the membrane. This molecular mobility is consistent with the observed linear dependence of the FWHM of the second Lorentzian on Q^2 (Fig. 4.16).

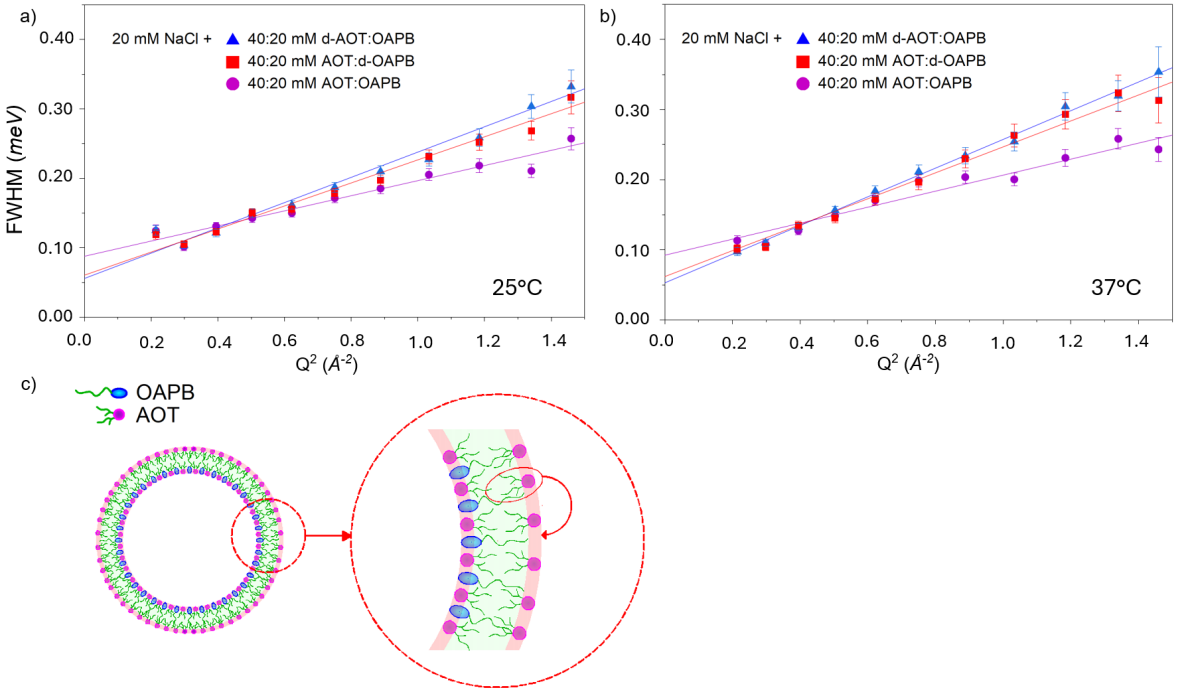

Figure 4.16: a) & b) Variation of the FWHM of the second Lorentzian as a function of Q^2 at different deuteration conditions; c) Schematic showing lateral diffusion of AOT surfactant molecule (pink) within the membrane surface.

According to Fick's law (Eq. 4.3), the intercept at $Q^2 = 0$ should be zero. However, this is not observed, as the FWHM intercept is related to the correlation time of internal motions associated with the second Lorentzian. Even at $Q^2 = 0$, the motion does not vanish because the system exhibits internal dynamics characterized by a finite correlation time, τ. These motions give rise to a minimum broadening of the spectrum. Consequently, the intercept is

shifted to higher values by a factor on the order of $1/\tau$ [51]. The diffusion coefficients (D_{lat}) associated with the lateral motion of the single surfactants were extracted and reported in Table 4.7.

Table 4.7: Lateral diffusion coefficients of surfactants within the membrane layer at different deuteration at 25 and 37 °C.

Composition	Isotope	T	$D_{eff} \cdot 10^9$	Error $\cdot 10^9$	τ	Error
		[°C]	[m^2/s]	[m^2/s]	[ps]	[ps]
40 mM d-AOT 20 mM OAPB 20 mM NaCl	D H -	25	1.38	0.07	23.5	4.3
		37	1.56	0.04	24.9	2.7
40 mM AOT 20 mM d-OAPB 20 mM NaCl	H D -	25	1.26	0.07	21.7	3.2
		37	1.41	0.08	21.2	4.0
40 mM AOT 20 mM OAPB 20 mM NaCl	H H -	25	0.83	0.06	15.0	1.4
		37	0.87	0.07	14.2	1.6

The two surfactants exhibit similar D_{lat} values within their respective error margin. One might expect AOT molecules to diffuse faster within the vesicle bilayer due to their smaller size (from Tanford $V_{AOT} = 565.4$ Å^3, $V_{OAPB} = 699.9$ Å^3) . However, AOT has a fully saturated double-tail structure, which can hinder its mobility. In addition, the negative charge of the head group is screened by the Na^+ counter-ions present in solution when NaCl is added, leading to denser packing of the AOT molecules. As a result, no significant difference is observed between the two surfactants, and both diffuse within the bilayer at comparable rates. Increasing temperature enhances the flexibility of the surfactant tails, weakening hydrophobic interactions and causing an increase in D_{lat}. When both surfactants are considered together, the measured D_{lat} decreases. This behaviour is approached in Section 4.2.4, when the apparently immobile fraction (p) is investigated. indicating a larger apparent immobile fraction within the instrumental resolution. This arises because the immobile contributions of both surfactant species are combined in the measured signal, thereby reducing the lateral diffusion coefficient. This interpretation can be supported by analysis of the EISF (discussed further in Section 4.2.4).

The contributions of both surfactants are also reflected in the shorter correlation times observed for the fully hydrogenated sample. A longer τ indicates that a single molecule remains in a particular state for longer before “changing” [52], which for this system would be before diffusing. The shorter correlation times obtained for the fully hydrogenated system is attributed to the fact that the measured QENS signal contains contributions from the hydrogen atoms of both surfactants. Consequently, the extracted correlation time represents an effective average over the local dynamics of both surfactant species, whereas in the selectively deuterated systems, the signal is dominated by only a single surfactant.

4.2.4. Confined motion of the surfactants

The variation of the Elastic Incoherent Structure Factor (EISF) with momentum transfer (Q) provides information about the geometry and spatial extent of molecular motion, and describes particles undergoing motion in restricted or confined spaces [53]. The EISF can be calculated

as shown in Eq. 4.7:

$$EISF = \frac{A_1}{A_1 + A_2} \tag{4.7}$$

where A_1 and A_2 are the amplitudes of the first and second Lorentzians, respectively. This ratio describes the relationship between the apparent immobile dynamics of the system and the total dynamics. Different models can be used to fit the EISF to understand the geometry and confinement of the observed motion [53]. In the case of AOT/OAPB vesicles, the model that best fits the obtained data and physically describes the system is the Gaussian confinement model (Eq. 4.8):

$$EISF = p + (1 - p) \cdot A \cdot \exp\left(-\frac{Q^2 \cdot \mathrm{MSD}}{3}\right) \tag{4.8}$$

where p is the apparently immobile fraction of hydrogen atoms, MSD is the mean squared displacement, and A is a correction factor that accounts for multiple scattering. Ideally, in a QENS experiment, neutrons interacting with the sample are scattered once before being detected. In this ideal case, $A = 1$. During a QENS experiment, however, neutrons can be scattered by a single nucleus and, before reaching the detector, interact with a subsequent nucleus. This phenomenon is known as multiple scattering, which typically results in a value for the factor A that is lower than 1.

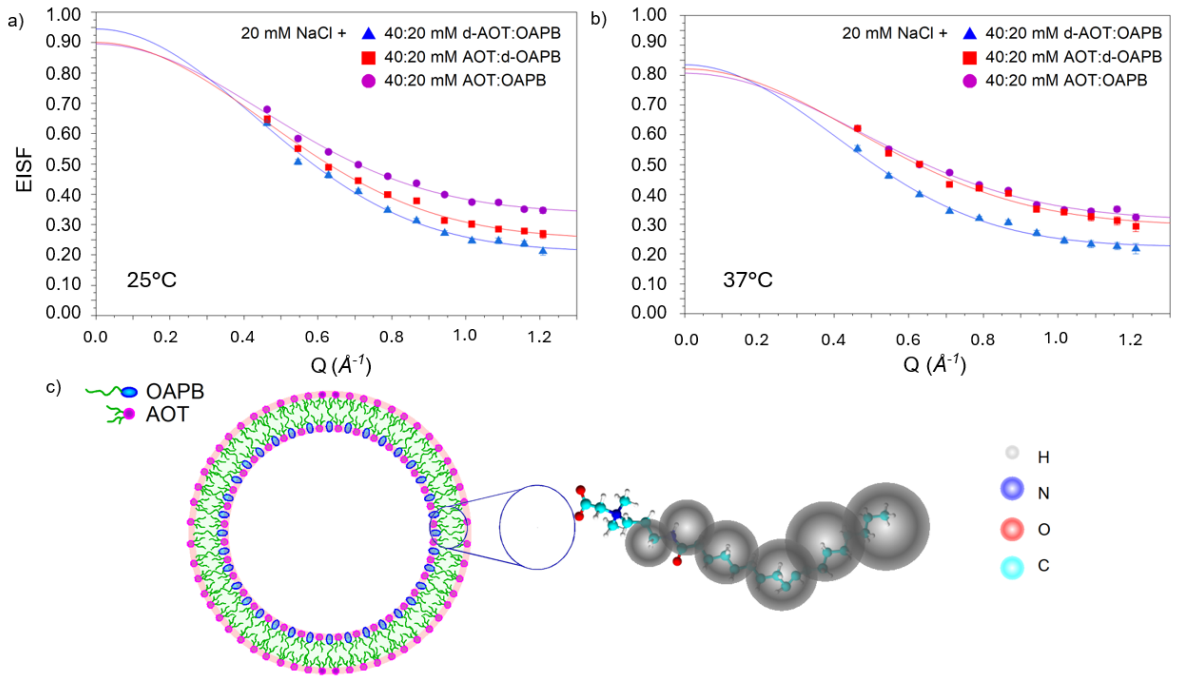

Figure 4.17: a) & b) Variation EISF as a function of Q at different deuteration conditions: a) 25°C, b) 37°C, c) Schematic model of Gaussian confinement for an OAPB molecule. Black spheres represent the probability confined volumes within which hydrogen atoms are moving.

Table 4.8: Confined Gaussian model parameters at different deuteration at 25 and 37°C.

Composition	Surfactant	T [°C]	MSD [Å^2]	Error [Å^2]	p	Error	A	Error
40 mM d-AOT 20 mM OAPB 20 mM NaCl	D H -	25	8.13	0.78	0.21	0.01	0.93	0.06
		37	9.24	1.01	0.22	0.01	0.79	0.07
40 mM AOT 20 mM d-OAPB 20 mM NaCl	H D -	25	7.40	0.88	0.26	0.02	0.84	0.06
		37	7.24	1.12	0.29	0.02	0.75	0.06
40 mM AOT 20 mM OAPB 20 mM NaCl	H H -	25	7.42	0.74	0.33	0.01	0.84	0.05
		37	7.00	0.85	0.32	0.01	0.72	0.05

Fig. 4.17 shows the model fits to the EISF for different deuterations, and the extracted parameters are reported in Table 4.8. The sketch in Fig. 4.17c illustrates the physical interpretation of the model. The neutron beam interacts with atomic nuclei and is scattered, with each atom or isotope characterized by a specific scattering cross section (σ). In organic systems such as AOT/OAPB, the signal arises predominantly from hydrogen nuclei, since the incoherent scattering cross section of hydrogen (σ_{inc}) is much larger than that of most other atoms or isotopes. Consequently, hydrogen atoms effectively act as a “label” for molecular dynamics.

Within the Gaussian confinement model, these hydrogen atoms are assumed to undergo localized motions within an effective Gaussian probability volume characterized by the mean square displacement (MSD). However, the hydrogen atoms are unable to move independently due to being covalently bonded to carbon atoms. Therefore, these motions are associated with the surfactant tails or with segments of these tails. The measured dynamics thus reflect the local flexibility and confinement of the chain segments. This also explains why at 37°C the MSD values remain comparable to values measured at 25°C within error margin. Although increasing temperature enhances the overall lateral diffusion of surfactant molecules in the bilayer, this does not necessarily increase the local confinement volume. In the temperature range considered, the internal geometry of the tail segments remains similar, without significant bond stretching or bond breaking.

A fraction of hydrogen atoms in the system appears to be immobile within the instrumental resolution. OAPB contains a double bond at the C9-10 position, which introduces stiffness and therefore hinders mobility. In addition, the OAPB headgroup interacts with AOT headgroups through electrostatic attraction between the quaternary ammonium group of OAPB, and the sulfonate group of AOT. This interaction leads to tighter surfactant packing, which likely restricts molecular motions due to confinement in the micelle structure.

However, AOT is also distributed in the outer layer of the vesicle system, where it interacts with free Na^+ ions in solution that act as charge screeners. This interaction also likely contributes to the slightly higher immobile fraction of hydrogen atoms observed for AOT, again due to packing confinement effects. When considering the contribution of both surfactants in the fully hydrogenated vesicle, the fraction of immobile hydrogen atoms reflects the combined contributions of both species, resulting in $p = 0.33 \pm 0.01$. This explains the differences in D_{lat} observed in Table 4.7.

4.2.5. SANS & QENS: relating structure to dynamics

The molecular dynamics probed by QENS were crucial for understanding the structural evolution and aggregate morphologies observed by SANS. Table 4.7 shows that the lateral diffusion coefficient (D_{lat}) of the surfactants increases when temperature increases to 37°C. When these results are compared with the SANS data shown in Fig. 4.4, a clear relationship emerges between molecular mobility and the observed vesicle to ellipsoidal micelle transition. The increased lateral diffusion of the surfactant molecules enhances the flexibility of the vesicle bilayer, reducing the effectiveness of the hydrophobic interactions that stabilize the packed membrane. As a result, the surfactants are able to reorganize into aggregates with a higher interfacial curvature, favouring the formation of ellipsoidal micelles. QENS therefore provides molecular insight for the structural transition identified by SANS.

The contrast variation SANS experiments further complement the QENS analysis by revealing an asymmetric distribution of the surfactants within the vesicle bilayer. The scattering signal originating predominantly from OAPB yielded a bilayer thickness of 1.36 ± 0.05 nm, compared with 2.23 ± 0.02 nm for the fully protonated system, and 2.32 ± 0.03 nm for the AOT highlighted system. These observations suggest that AOT is distributed throughout both leaflets of the bilayer, whereas OAPB is concentrated predominantly within a single leaflet. This structural model also provides an explanation for the slightly higher apparent immobile fraction (p) measured for AOT. In addition to the interactions between the headgroups and hydrocarbon tails of both surfactants, the AOT molecules located in the outer leaflet experience electrostatic screening by free Na^+ ions in solution. This screening promotes tighter molecular packing, resulting in a larger fraction of apparently immobile hydrogen atoms associated with AOT.

Finally, the bilayer thickness determined from the OAPB contrast variation experiment (1.36 ± 0.05 nm) is smaller than the fully extended chain length of OAPB (from Tanford $l_{\mathrm{c}} = 2.43$ nm). The confined motions obtained from the Elastic Incoherent Structure Factor analysis provide a molecular explanation for this observation. The confined diffusion model indicates that the surfactant hydrocarbon chains remain flexible within the bilayer rather than adopting fully extended conformations. Consequently, the chains continuously explore a confined volume through localized motions, giving rise to an average bilayer thickness that is smaller than the molecular length measured for an extended surfactant molecule. Given these finding it is apparent that QENS and SANS results provide complementary dataset linking molecular flexibility and motions to the nanoscale structure of the vesicle membrane.

5

Conclusions and Future Recommendations

This work investigated the self-assembly of mixed OAPB/AOT surfactant systems in aqueous solution by combining small angle neutron scattering (SANS), quasi elastic neutron scattering (QENS), dynamic light scattering (DLS), zeta potential measurements, and selective deuteration.

SANS measurements demonstrated that the morphology of the OAPB/AOT system is sensitive to electrostatic interactions. In the absence of NaCl, the scattering data were well described by charged ellipsoidal micelles interacting through a Hayter-Penfold structure factor. Upon the addition of 20 mM NaCl, the electrostatic repulsion between the surfactant headgroups was shielded, reducing aggregate curvature and promoting the spontaneous formation of unilamellar vesicles, with an average radius of 19.40 nm. Zeta potential measurements confirmed charge screening effects with a reduction in the magnitude of zeta potential from 85.20 mV to 36.77 mV upon salt addition.

Contrast variation showed that both surfactants are present within ellipsoidal micelles, as no significant changes in aggregate dimensions were observed when either component was selectively deuterated. For vesicular systems, contrast variation revealed differences in the fitted bilayer thicknesses. The fully protonated sample and sample with deuterated OAPB exhibited comparable bilayer thicknesses, whereas the sample in which scattering originated manly from OAPB displayed a thinner membrane. These results suggest that AOT is distributed throughout both leaflets of the bilayer, while OAPB is predominantly located within one leaflet, presumably the inner one given that the determined vesicle size was smaller for contrast-matched AOT (d_{34}-AOT) than the other two samples.

Temperature was found to strongly influence system self-assembly. Increasing the temperature destabilized the vesicular morphology, leading to the coexistence of both vesicles and ellipsoidal micelles at 37°C, followed by a complete transition to ellipsoidal micelles at 50°C. The coexistence of vesicle and ellipsoidal micelles at 37°C, between the vesicular state at 25°C and the ellipsoidal micellar state at 50°C, suggests that the structural transition occur over a finite temperature range rather than a well defined transition temperature. Selective deuteration further demonstrated that the ellipsoidal micelles are not formed by one surfactant only, but rather result from the contribution of both surfactants, highlighting the potential of mixed surfactant systems in the formation of complex morphologies.

QENS measurements provide insight into the molecular motions underpinning these structural changes. Analysis of the quasi elastic spectra resolved distinct dynamic processes: Brownian diffusion of the full aggregates, lateral diffusion of surfactant molecules within the membrane, and localized confined motions of the surfactant chains. DLS measurements complemented the QENS data obtained for vesicle diffusion, and helped demonstrate that QENS probes both translational and rotational diffusion which cannot be indipendently isolated due to comparable timescales. In addition, the lateral diffusion coefficients for the surfactant molecules increase with temperature, demonstrating that surfactant mobility within the membrane becomes progressively faster as thermal energy increases. This enhanced molecular mobility provides an insight for the structural evolution observed by SANS: as the surfactants diffuse more rapidly within the membrane, the hydrophobic interactions and charge screening effects that stabilize the vesicular bilayer become less effective, allowing the aggregates to reorganize into structures with higher curvature. Therefore, QENS provides fundamental insight on the mechanism of the vesicle to ellipsoidal micelle transition observed by SANS.

The confined motions obtained from the elastic incoherent structure factor analysis further complement the structural observations. The confined diffusion model indicates that the surfactant chains remain flexible within the aggregates rather than adopting rigid conformations. This molecular flexibility is consistent with the relatively small bilayer thickness obtained from the SANS analysis.

Taken together, the SANS and QENS results demonstrate that the morphology of the OAPB/AOT system is governed not only by electrostatic interactions, but also by the underlying molecular dynamics. SANS establishes which structures are formed under different conditions, whereas QENS reveals the molecular processes responsible for stabilizing or transforming those structures. The two techniques therefore provide complementary information that cannot be obtained by either independently: the structural transitions observed by SANS are directly linked to changes in surfactant mobility measured by QENS.

More broadly, these results demonstrate the potential of mixed surfactant systems to access complex and tunable self-assembled structures, while highlighting the value of combining complementary techniques such as SANS, QENS, DLS, zeta potential measurements, and selective deuteration to establish direct links between molecular interactions, dynamics, and macroscopic aggregate morphology.

5.1. Future research recommendations

This work provides a basis for further research that could both complement the present study and extend its scope to a broader range of research questions:

- Appendix H shows the QENS data fits obtained for the dynamics of the OAPB/AOT mixed surfactant system without salt. The dataset is incomplete. To obtain a more comprehensive understanding of the system dynamics and complement the SANS results, the missing samples, AOT:OAPB at 37 °C, d-AOT/OAPB at both 25 and 37 °C, and possibly AOT/d-OAPB at 37 °C (as this sample was not measured for a sufficiently long time, should be measured using QENS). This would allow for a full comparison of the molecular dynamics and a complete understanding of the effects of salt, with a direct link to the structural features observed by SANS.
- Molecular Dynamics (MD) simulations could be performed to compute molecular trajectories and provide a mechanistic interpretation of the QENS results [10]. Specifically, the force fields for both surfactants, including their interaction potential parameters, would

be required. The main challenge with this approach is that, although force field parameters for AOT can be found in the literature, to the best of my knowledge, no force field for OAPB has been reported. Therefore, a force field for OAPB would first need to be developed, before simulation can take place.

- In the case that the studied system could be used for encapsulation applications, such as drug delivery, it would be important to investigate its behaviour under physiological salt concentrations (150 mM) [54]. Now that the system stability, dynamics, and morphology have been characterized, it would be particularly relevant to determine whether the vesicle to ellipsoidal micelles transition, which would represent the key release mechanism, still occurs at higher temperatures (either 37 or 50°C). If this transition occurs under these conditions, several further research questions could be explored, including the stability of the vesicles in the bloodstream, the encapsulation of different drugs within the vesicles, and the kinetics and efficiency of drug release.
- Substituting OAPB with other, less expensive betaine surfactants could be interesting for investigating the effects of chain length and saturation on vesicle assembly, while also reducing costs. One possible alternative is cocamidopropyl betaine (CAPB, $C_{19}H_{38}N_2O_3$). a precursor in the synthesis of OAPB. CAPB is a naturally derivedblended surfactant mixture which possesses shorter, mainly fully saturated hydrocarbon chains than OAPB[55]. The absence of a double bond is expected to improve the packing of the surfactant molecules by increasing the contact area and, consequently, van der Waals interactions [**McCoyorganicadd**]. This could potentially promote vesicle formation even in the absence of added salt. It would therefore be interesting to investigate whether the vesicles formed under these conditions would also undergo a transition to ellipsoidal micelles.
- Section 4.2.2 explores the possibility that the observed differences between deuterated and protonated samples arise from isotope effects associated with the lower zero-point vibrational energy of deuterium compared to hydrogen. These differences could, as a consequence, affect the interactions between the surfactant tails and thereby contribute to the differences in structures and dynamics observed between deuterated and protonated samples. To directly determine whether deuteration leads to differences in the instantaneous dipole moments, and consequently in the London dispersion forces between the hydrocarbon tails, would be experimentally challenging. Therefore, an alternative approach is to probe the consequences of these interactions indirectly by comparing the interfacial properties of deuterated and protonated surfactant layers. One possible approach is oscillating drop tensiometry, which can be used to investigate the dilatational response of the interface [56]. A higher membrane stiffness, as discussed in Section 4.2.2, is expected to result in a larger elastic modulus, since a larger change in interfacial tension is required to accommodate a given relative change in area. Thus, a larger elastic modulus indicates a greater resistance of the surfactant layer to deformation [56].
- Appendix E shows that at 10°C, the mixed surfactant system exhibits a periodic lamellar structure. To visualize this structure, polarized optical microscopy can be used to provide direct information about the alignment of the structure [57]. Under polarized light, the system may display a range of different colors due to the material's optical birefringence, which arises from the difference between the refractive indices parallel and perpendicular to the structural alignment [57].

References

[1] Milton J. Rosen. *Surfactants and interfacial phenomena*. en. Third edition. A Wiley-Interscience publication. Hoboken, N.J: Wiley-Interscience, 2010.

[2] J. Kobierski et al. “Predicting the packing parameter for lipids in monolayers with the use of molecular dynamics”. In: *Colloids and Surfaces B: Biointerfaces* 211 (Mar. 2022).

[3] L. S. Laurier, N. S. Elaine, and M. D. Gerrard. “Surfactants and Their Applications”. In: *Annual Reports Section ”C” (Physical Chemistry)* 99 (2003), pp. 3–48.

[4] A. Khan and E. F. Marques. “Synergism and polymorphism in mixed surfactant systems”. In: *Current Opinion in Colloid & Interface Science* 4.6 (Dec. 1999), pp. 402–410.

[5] T. M. McCoy et al. “The effects of small molecule organic additives on the self-assembly and rheology of betaine wormlike micellar fluids”. In: *Journal of Colloid and Interface Science* 534 (Jan. 2019), pp. 518–532.

[6] L. Arleth and J. S. Pedersen. “Droplet polydispersity and shape fluctuations in AOT [bis(2-ethylhexyl)sulfosuccinate sodium salt] microemulsions studied by contrast variation small-angle neutron scattering”. In: *Physical Review E* 63.6 (May 2001).

[7] Thomas M. McCoy et al. “Spontaneous Self-Assembly of Thermoresponsive Vesicles Using a Zwitterionic and an Anionic Surfactant”. In: *Biomacromolecules* 21.11 (Nov. 2020), pp. 4569–4576.

[8] S. Ghosh, A. Ray, and N. Pramanik. “Self-assembly of surfactants: An overview on general aspects of amphiphiles”. In: *Biophysical Chemistry* 265 (Oct. 2020), p. 106429.

[9] M. J. Hollamby. “Practical applications of small-angle neutron scattering”. In: *Physical Chemistry Chemical Physics* 15.26 (2013), pp. 10566–10579.

[10] V. K. Sharma, S. Mitra, and R. Mukhopadhyay. “Dynamic Landscape in Self-Assembled Surfactant Aggregates”. In: *Langmuir* 35.44 (Nov. 2019), pp. 14151–14172.

[11] S. M. Saini et al. “Brief overview of surfactants, properties, classification, passivation, and role in chemistry”. In: *Surfactant Based Electrochemical Sensors and Biosensors*. Elsevier, 2024, pp. 3–20.

[12] D. R. Perinelli et al. “Surfactant Self-Assembling and Critical Micelle Concentration: One Approach Fits All?” In: *Langmuir* 36.21 (June 2020), pp. 5745–5753.

[13] S. Perumal, R. A., and W. Lee. “A Review of Polymeric Micelles and Their Applications”. In: *Polymers* 14.12 (June 2022).

[14] C. Tanford. *The Hydrophobic Effect: Formation of Micelles and Biological Membranes*. 2nd. New York: Wiley, 1980.

[15] S. Svenson. “Controlling surfactant self-assembly”. In: *Current Opinion in Colloid & Interface Science* 9.3-4 (Nov. 2004), pp. 201–212.

[16] F. Cousin. “Small angle neutron scattering”. In: *EPJ Web of Conferences* 104 (2015). Ed. by M. Ceretti et al.

[17] A. J. Jackson. *Introduction to Small-Angle Neutron Scattering and Neutron Reflectometry*. May 2008.

[18] E. M. A. Hussein. “Cross Sections”. In: *Radiation Mechanics*. Elsevier, 2007. Chap. 3.

[19] D. S. Schmool and H. Kachkachi. “Collective Effects in Assemblies of Magnetic Nanoparticles”. In: *Solid State Physics*. Vol. 67. Academic Press, 2016, pp. 1–101.

[20] National Institute of Standards and Technology. *Neutron Scattering Lengths and Cross Sections*. 2026. URL: https://www.ncnr.nist.gov/resources/n-lengths/list.html.

[21] B Jacrot. “The study of biological structures by neutron scattering from solution”. In: *Reports on Progress in Physics* 39.10 (Oct. 1976), pp. 911–953.

[22] D. Lombardo, P. Calandra, and M. A. Kiselev. “Structural Characterization of Biomaterials by Means of Small Angle X-rays and Neutron Scattering (SAXS and SANS), and Light Scattering Experiments”. In: *Molecules* 25.23 (Nov. 2020), pp. 5624–5661.

[23] V. G. Sakai and A. Arbe. “Quasielastic neutron scattering in soft matter”. en. In: *Current Opinion in Colloid & Interface Science* 14.6 (Dec. 2009), pp. 381–390.

[24] G. E. Pérez et al. “Neutron and muon characterisation techniques for battery materials”. In: *Journal of Materials Chemistry A* 11.20 (2023), pp. 10493–10531.

[25] ISIS Neutron and Muon Source. *IRIS instrument*. https://www.isis.stfc.ac.uk/instruments/iris/. n.d. DOI: 10.5286/ISIS.IRIS.RB2420476.

[26] H. Fritzsche, J. Huot, and D. Fruchart, eds. *Neutron Scattering and Other Nuclear Techniques for Hydrogen in Materials*. Neutron Scattering Applications and Techniques. Cham: Springer International Publishing, 2016.

[27] T. Springer and R. E. Lechner. “Diffusion Studies of Solids by Quasielastic Neutron Scattering”. en. In: *Diffusion in Condensed Matter*. Ed. by P. Heitjans and J. Kärger. Berlin/Heidelberg: Springer-Verlag, 2005, pp. 93–164.

[28] A. Kusmin, R. E. Lechner, and W. Saenger. “Quasielastic small-angle neutron scattering from heavy water solutions of cyclodextrins”. In: *The Journal of Chemical Physics* 134.2 (Jan. 2011).

[29] P. A. Hassan, S. Rana, and G. Verma. “Making Sense of Brownian Motion: Colloid Characterization by Dynamic Light Scattering”. In: *Langmuir* 31.1 (Jan. 2015), pp. 3–12.

[30] ISIS Neutron and Muon Source. *Larmor instrument*. https://www.isis.stfc.ac.uk/instruments/larmor/. n.d. DOI: 10.5286/ISIS.LARMOR.RB2669001.

[31] SasView Project. *SasView: Small Angle Scattering Analysis*. 2026. URL: https://www.sasview.org/.

[32] Mantid Project. *Mantid Workbench Documentation*. 2026. URL: https://docs.mantidproject.org/nightly/workbench/index.html.

[33] T. L. Doane et al. “Nanoparticle ζ -Potentials”. In: *Accounts of Chemical Research* 45.3 (Mar. 2012), pp. 317–326.

[34] J. Eastoe et al. “Small-angle neutron scattering from novel bis-2- ethylhexylsulphosuccinate microemulsions: evidence for non-spherical structures”. In: *Physica B: Condensed Matter* 180-181 (June 1992), pp. 555–557.

[35] C. G. De Kruif et al. “Hard-sphere colloidal silica dispersions. The structure factor determined with SANS”. In: *Langmuir* 4.3 (May 1988), pp. 668–676.

[36] E. G. Kelley et al. “Interactions, Diffusion, and Membrane Fluctuations in Concentrated Unilamellar Lipid Vesicle Solutions”. In: *Frontiers in Physics* 10 (Apr. 2022).

[37] S. Manet et al. “Structure of Bolaamphiphile Sophorolipid Micelles Characterized with SAXS, SANS, and MD Simulations”. In: *The Journal of Physical Chemistry B* 119.41 (Oct. 2015), pp. 13113–13133.

[38] S. Prakash and J. Yeom. “Fundamentals for Microscale and Nanoscale Flows”. In: *Nanofluidics and Microfluidics*. Elsevier, 2014, pp. 9–38.

[39] Benton B. Owen et al. “THE DIELECTRIC CONSTANT OF WATER AS A FUNCTION OF TEMPERATURE AND PRESSURE[1,2]”. In: *The Journal of Physical Chemistry* 65.11 (Nov. 1961), pp. 2065–2070.

[40] I. P. Silverwood et al. *The IRIS User Guide, 5th ed.* Tech. rep. STFC, 2025.

[41] M. Sarter et al. “Data Analysis of Dynamics in Protein Solutions Using Quasi-Elastic Neutron Scattering─Important Insights from Polarized Neutrons”. In: *Journal of the American Chemical Society* (Oct. 2024).

[42] G. Paradossi et al. “Supercooled Water in PVA Matrixes: I. An Incoherent Quasi-Elastic Neutron Scattering (QENS) Study”. In: *The Journal of Physical Chemistry B* 107.33 (Aug. 2003), pp. 8363–8371.

[43] National Institute of Standards and Technology. *Atomic Weights and Isotopic Compositions for All Elements*. 2025. URL: `https://physics.nist.gov/cgi-bin/Compositions/stand_alone.pl`.

[44] C. H. Chen. *Deuterium Oxide and Deuteration in Biosciences*. Cham: Springer International Publishing, 2022.

[45] Karl K. Irikura. “Experimental Vibrational Zero-Point Energies: Diatomic Molecules”. In: *Journal of Physical and Chemical Reference Data* 36.2 (June 2007), pp. 389–397.

[46] A. R. Ubbelohde. “Zero point energy in the determination of the structure of solids”. In: *Transactions of the Faraday Society* 32 (1936), pp. 525–529.

[47] Chenxing Liang, Archith Rayabharam, and N. R. Aluru. “Structural and Dynamical Properties of H_2 O and D_2 O under Confinement”. In: *The Journal of Physical Chemistry B* 127.29 (July 2023), pp. 6532–6542.

[48] C. L. Perrin and Y. Dong. “Secondary Deuterium Isotope Effects on the Acidity of Carboxylic Acids and Phenols”. In: *Journal of the American Chemical Society* 129.14 (Apr. 2007), pp. 4490–4497.

[49] L. Sobczyk, M. Obrzud, and A. Filarowski. “H/D Isotope Effects in Hydrogen Bonded Systems”. In: *Molecules* 18.4 (Apr. 2013).

[50] K. Gong et al. “*In situ* quasi-elastic neutron scattering study on the water dynamics and reaction mechanisms in alkali-activated slags”. In: *Physical Chemistry Chemical Physics* 21.20 (2019), pp. 10277–10292.

[51] M. Grimaldo et al. “Hierarchical molecular dynamics of bovine serum albumin in concentrated aqueous solution below and above thermal denaturation”. In: *Physical Chemistry Chemical Physics* 17.6 (2015), pp. 4645–4655.

[52] A. Tokmakoff. “Time Dependent Quantum Mechanics and Spectroscopy”. en. In: (2026), pp. 120–138.

[53] M. Bée. “A physical insight into the elastic incoherent structure factor”. In: *Physica B: Condensed Matter* 182.4 (Dec. 1992), pp. 323–336.

[54] M. Almagor and R. D. Cole. “In Physiological Salt Conditions the Core Proteins of the Nucleosomes in Large Chromatin Fragments Denature at 73 °C and the DNA Unstacks at 85 °C”. In: *Journal of Biological Chemistry* 264.11 (Apr. 1989), pp. 6515–6519.

[55] D. Kim et al. “Safety assessment of cocamidopropyl betaine, a cosmetic ingredient”. In: *Toxicological Research* 40.3 (July 2024), pp. 361–375.

[56] E.M. Freer, H. Wong, and C.J. Radke. “Oscillating drop/bubble tensiometry: effect of viscous forces on the measurement of interfacial tension”. In: *Journal of Colloid and Interface Science* 282.1 (Feb. 2005), pp. 128–132.

[57] C. Chen et al. “LCPOM: Precise Reconstruction of Polarized Optical Microscopy Images of Liquid Crystals”. In: *Chemistry of Materials* 36.7 (Apr. 2024), pp. 3081–3091.

[58] M. C. Holmes, M. S. Leaver, and A. M. Smith. “Nematic and Disrupted Lamellar Phases in Cesium Pentadecafluorooctanoate/2H2O: A Small Angle Scattering Study”. In: *Langmuir* 11.1 (Jan. 1995), pp. 356–365.

[59] R. A. L. Jones. *Soft Condensed Matter*. Vol. 6. Oxford Master Series in Physics. Oxford University Press, 2002.

[60] N. Haridasan et al. “Rotational Diffusion of Proteins in Nanochannels”. In: *The Journal of Physical Chemistry B* 123.23 (June 2019), pp. 4825–4832.

[61] S. E. Braslavsky. “Glossary of terms used in photochemistry, 3rd edition (IUPAC Recommendations 2006)”. In: *Pure and Applied Chemistry* 79.3 (Jan. 2007), pp. 293–465.

A

Size difference observed between deuterated vesicle systems

Fig. 4.2b and table 4.1 showed that there is a difference in the vesicle radii between the deuterated and hydrogenated samples, exceeding the bilayer thickness. This led to the hypothesis that this surfactant mixture is more sensitive to preparation conditions than previously known, making it difficult to obtain vesicles of the same size within the experimental error each time the samples are prepared. To confirm this, additional SANS fits obtained at different times (corresponding to another batch of samples, measured a one week after preparation) are shown below.

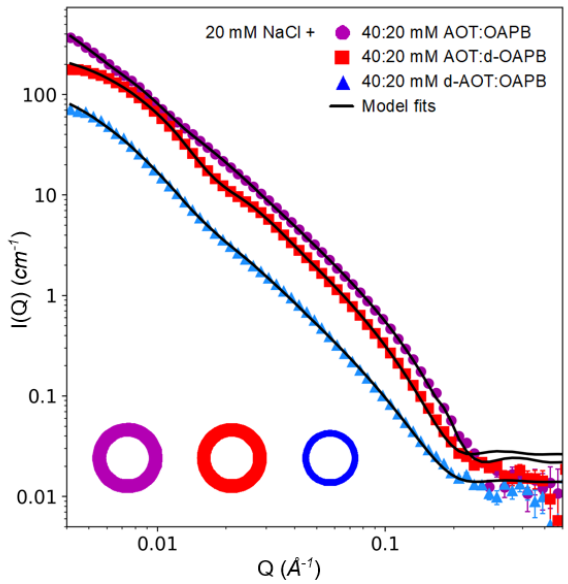

Figure A.1: SANS data and model fits of mixed OAPB and AOT solution (20 mM:40 mM respectively) and 20mM NaCl with non deuterated surfactants (purple), deuterated OAPB (red) and deuterated AOT (blue), with a schematic representation highlighting the region of the vesicle bilayer responsible for the SANS signal, corresponding to the non deuterated component.

Table A.1: SANS model parameters for 20 mM OAPB and 40 mM AOT with 20 mM NaCl and different surfactants deuteration at 25°C.

Composition	Model	R_v [nm]	PD (R_v) [%]	Thickness$_v$ [nm]	ϕ_v [%]
40 mM AOT 20 mM OAPB 20 mM NaCl	V	21.42 ±0.04	38.5 ±0.1	2.30 ±0.02	16.70 ±0.73
40 mM d-AOT 20 mM OAPB 20 mM NaCl	V	15.02 ±0.06	42.6 ±0.3	2.52 ±0.01	6.60 ±0.10
40 mM AOT 20 mM d-OAPB 20 mM NaCl	V	14.27 ±0.02	33.4 ±0.1	2.66 ±0.05	10.11 ±0.04

Owing to the high polydispersity of the systems, which smooths the scattering curves, differences in size are observed among the various deuteration conditions. Furthermore, the fitted radii do not follow the same trend as that reported in table A.1, ruling out the possibility that the observed differences arise from the use of deuterated surfactants, for example because of impurities or incomplete desalting. These results suggest that the mixed surfactant system assembles into the same type of aggregates, but that their size is difficult to reproduce consistently. This behavior may originate either from variations in the sample preparation procedure or from the strong sensitivity of the system to the surfactant concentration in solution.

Finally, DLS measurements revealed that the kinetics of vesicle assembly in solution evolve over time. As shown in Fig. A.2, one month after sample preparation the diffusion became faster, indicating a corresponding change in vesicle size.

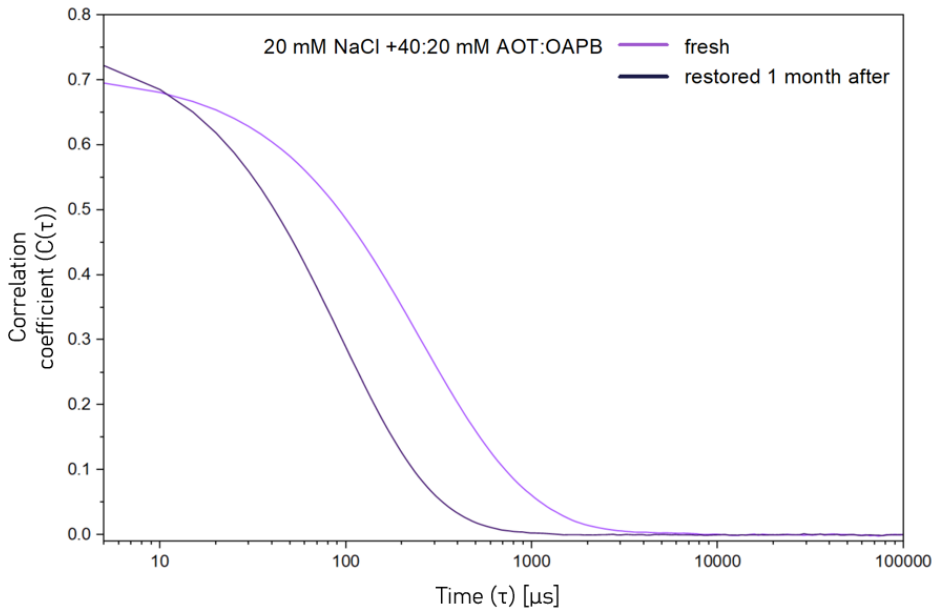

Figure A.2: DLS correlation function for AOT:OAPB 40:20 mM with 20 mM NaCl for fresh sample (light purple) and sample measured after 1 month (dark purple) at 25○C.

It should be noted that samples stored for extended periods begin to exhibit phase separation. Consequently, before the DLS measurements were performed after one month, the samples required additional stirring and sonication to restore a homogeneous dispersion. This sample treatment should be considered when interpreting the observed changes in the diffusion coefficient and vesicle size.

B

Surfactant deuteration fitting parameters at 37°C

Table B.1: SANS model parameters for 20 mM d-OAPB and 40 mM AOT with 20 mM NaCl at 37°C for a combined core shell+ellipsoid model.

Composition	Model	$R_{eq.}$ [nm]	R_p [nm]	Charge [e]	ϕ_e [%]	R_v [nm]	PD (R_v) [%]	Thickness$_v$ [nm]	ϕ_v [%]
40 mM AOT 20 mM d-OAPB 20 mM NaCl	V+E	2.15 ±0.03	9.03 ±0.61	–	–	25.47 ±0.17	30.6 ±0.5	2.34 ±0.21	–
40 mM d-AOT 20 mM OAPB 20 mM NaCl	V+E	1.79 ±0.16	5.68 ±0.26	–	–	13.18 ±0.71	23.9 ±0.5	1.91 ±1.40	–

C

Dilution series fitting parameters

Table C.1: SANS model parameters for OAPB and AOT ellipsoids at a fixed surfactant ratio (2:1, AOT:OAPB) at 25 and 37°C. Hayter-Penfold Structure factor was used for the fit.

AOT:OAPB [mM]	T [°C]	Model	$R_eq.$ [nm]	R_p [nm]	Charge [e]	ϕ_e [%]
40:20	25	E	1.88±0.01	3.26±0.04	34.2±2.3	2.06±0.03
	37		1.86±0.01	3.16±0.05	32.4±2.1	2.10±0.03
35:17.5	25	E	1.89 ±0.02	3.17±0.05	28.6±1.9	1.89±0.03
	37		1.87±0.02	3.09±0.05	30.2±2.1	1.87±0.02
30:15	25	E	1.87±0.02	3.11±0.05	28.9±2.2	1.56±0.03
	37		1.89±0.02	2.95±0.06	28.1±2.2	1.57±0.03
25:12.5	25	E	1.89±0.02	3.03± 0.06	27.8±2.5	1.33±0.03
	37		1.76±0.02	3.12±0.05	24.0±1.9	1.29±0.03
20:10	25	E	1.89±0.03	2.88± 0.08	26.0±2.9	1.00±0.02
	37		1.88±0.04	2.85±0.08	26.2±3.0	1.04 ±0.02

D

Cooling down memory effects

SANS data were also collected for the mixed surfactant system after reaching 50°C (Fig. 4.4) and after subsequently cooling the system back to 10°C. Fig. D.1 shows that, after reaching 50°C, the system appears to retain a memory of the ellipsoidal micelles formed at this temperature, with these structures coexisting with other micellar structures. Furthermore, in the deuterated system, the surfactants exhibit different scattering signals, suggesting that they may have undergone partial separation in solution following the heating cycle. The coexistence of micelles with different topologies prevented reliable fitting of the dataset.

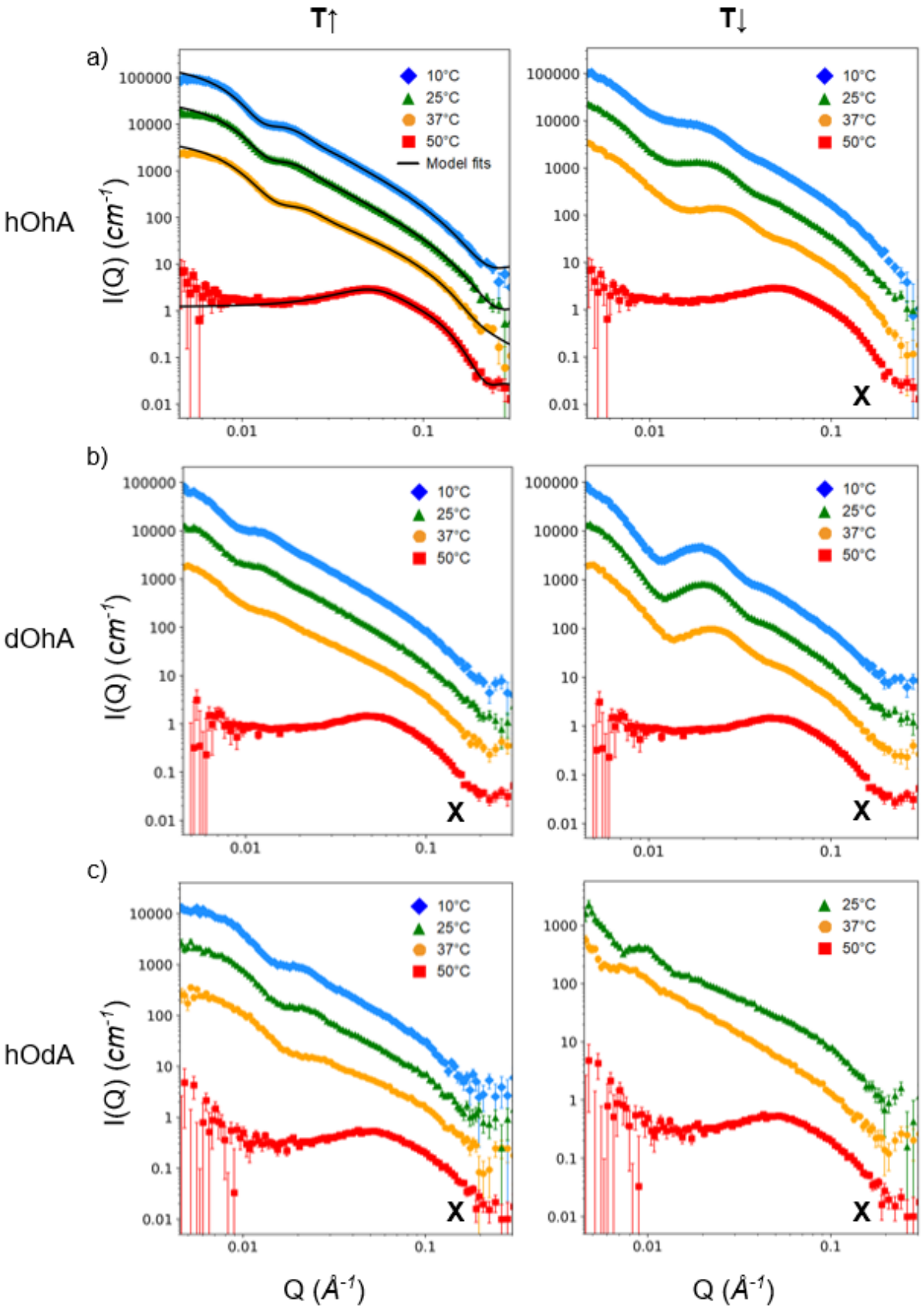

Figure D.1: SANS data point for temperature ramp going up from 10 to 50°C (left) and back down to 10°C (right) for a) 20 mM OAPB and 40 mM AOT with 20 mM NaCl (hOhA); b) 20 mM d-OAPB and 40 mM AOT with 20 mM NaCl (dOhA); c) 20 mM OAPB and 40 mM d-AOT with 20 mM NaCl (hOdA). X = unfit.

E

Crystallization at lower temperatures

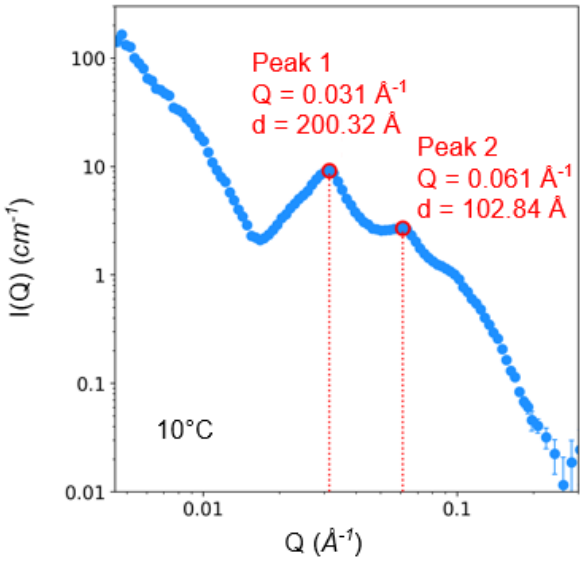

Figure E.1: SANS data of mixed OAPB and AOT solution (20 mM:40 mM respectively) at 10°C.

Fig. E.1 shows the SANS profile of the OAPB/AOT mixed surfactant system at 10 °C. No suitable model was found to adequately describe the experimental data. However, two distinct correlation peaks were identified at $Q_1 = 0.031$ Å^{-1} and $Q_2 = 0.061$ Å^{-1}, corresponding to d-spacings of $d_1 = 200.32$ Å and $d_2 = 102.84$ Å, respectively, according to Eq. E.1:

$$d = \frac{2\pi}{Q}. \tag{E.1}$$

The ratio $Q_2/Q_1 \approx 2$ indicates a periodically ordered, lamellar structure [58].

F

Core-shell and core multi-shell models

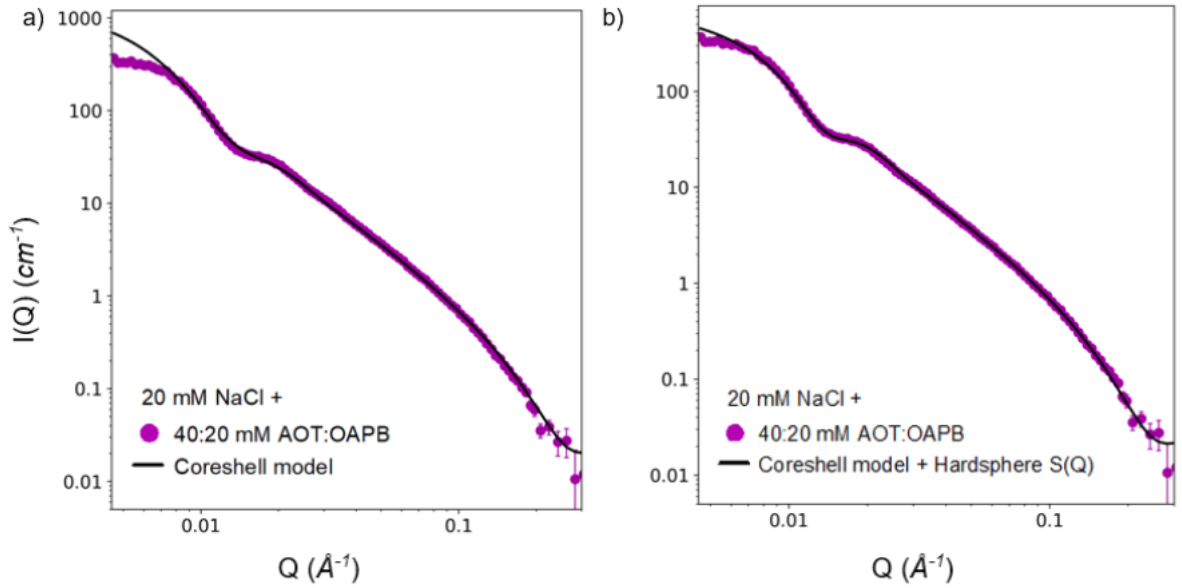

Figure F.1: SANS data of mixed OAPB and AOT solution (20 mM:40 mM respectively) and 20 mM NaCl at 25°C using a) coreshell model without any structure factor; b) core shell model with hardsphere structure factor. The red circles highlight the bigger mismatch between data and model fit when no structure factor is used.

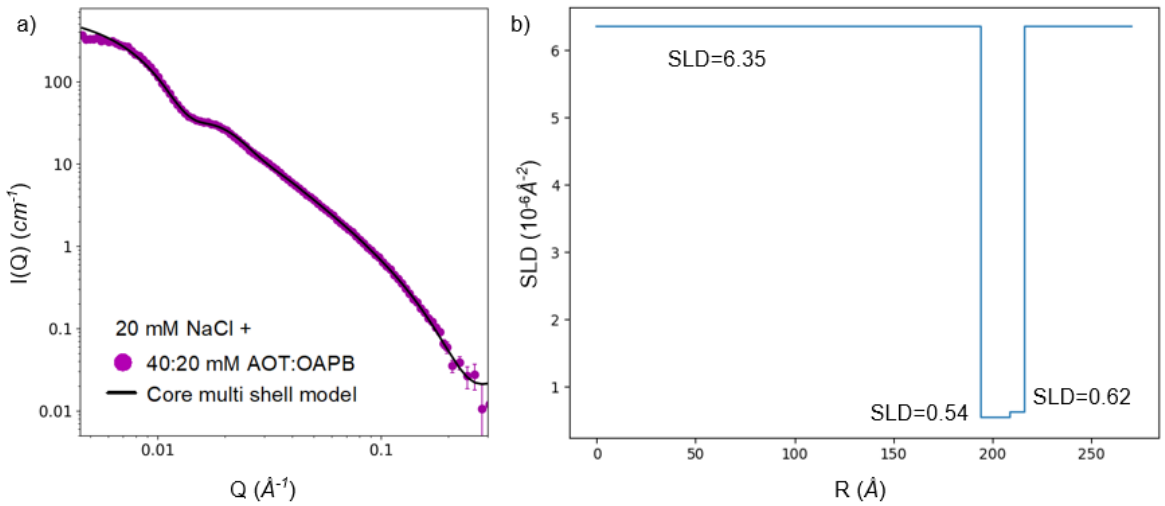

Figure F.2: a) SANS data and core-multishell model of mixed OAPB and AOT solution (20 mM:40 mM respectively) and 20 mM NaCl at 25°C; b) SLD profile distribution inside the vesicle where $SLD_{98\%D_2O} = 6.35 \cdot 10^{-6}$Å^{-2}, $SLD_{OAPB+AOT} = 0.54 \cdot 10^{-6}$Å^{-2}, and $SLD_{AOT} = 0.62 \cdot 10^{-6}$Å^{-2} (Fig. 4.3). The SLD distribution plot shows how in the inner leaflet there is likely a distribution of AOT and OAPB, while in the outer leaflet only AOT is present.

Table F.1: SANS model parameters for 20 mM OAPB and 40 mM AOT with 20 mM NaCl using coreshell model with no structure factor and a core multi-shell model with hard sphere structure factor.

Composition	Model	S(Q)	R_v [nm]	PD (R_v) [%]	Thickness$_1$ [nm]	Thickness$_2$ [nm]	ϕ_v [%]
40 mM AOT 20 mM OAPB 20 mM NaCl	Coreshell	-	19.06 ±0.05	30.0 ±0.2	2.07 ±0.10	-	9.80 ±0.08
40 mM AOT 20 mM OAPB 20 mM NaCl	Core multi-shell	HS	19.40 ±0.21	25.0 ±0.3	1.49 ±46.28*	0.74 ±46.06*	9.23 ±0.14

*The reported errors are not realistic because the thicknesses are correlated, and the core multi-shell model cannot uniquely determine them

G

Characteristic time comparison between rotational and Brownian diffusion.

QENS cannot always distinguish between rotational and Brownian diffusion, since both dynamics occur on comparable timescales and their contribution in the energy spectrum may overlap.

As described in this work, Brownian diffusion follows the Stokes-Einstein equation (eq. 4.4). The diffusion coefficient is derived from the assumption of a random walk, for which the mean displacement is always zero, whereas the mean square displacement in three dimensions is given by [59]:

$$\langle R^2 \rangle = \frac{k_B T}{\pi \eta R} t \tag{G.1}$$

Substituting Eq. 4.4 into Eq. G.1 yields the characteristic time required for a spherical particle to diffuse over a distance equal to its own radius, (R):

$$t \propto R^3 \tag{G.2}$$

In comparison, the rotational diffusion of a colloidal particle can be related to its size through the Stokes-Einstein-Debye equation [60]:

$$D_r = \frac{k_B T}{8 \pi \eta R_h^3} \tag{G.3}$$

The characteristic time associated with the reorientation of a spherical particle in a homogeneous fluid is given by [61]

$$t_r = \frac{1}{6 D_r} \tag{G.4}$$

which leads to

$$t_r \propto R^3. \tag{G.5}$$

In the present system, QENS cannot distinguish between translational and rotational diffusion because both processes occur on comparable timescales and are expected to contribute within the instrumental resolution

H

Supplementary QENS data

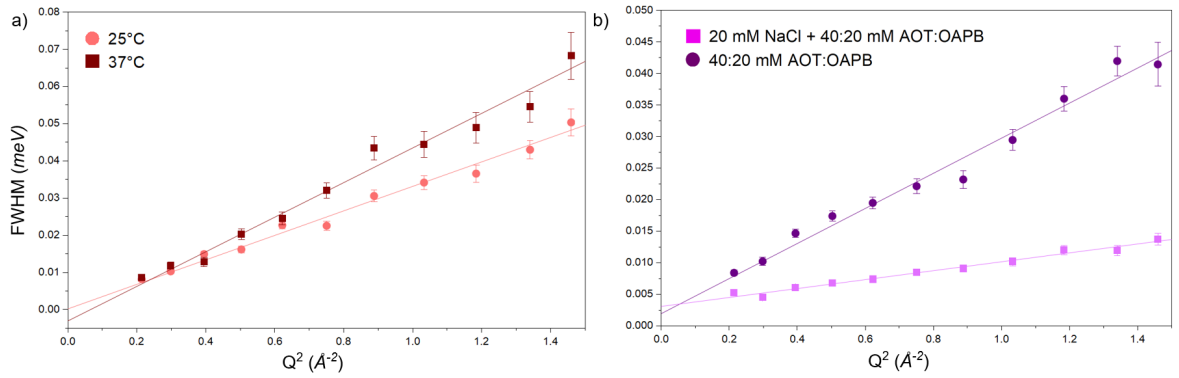

Figure H.1: Variation of the FWHM of the first Lorentzian as a function of Q^2 for a) 40:20 mM AOT:(deuterated)OAPB without salt addition at 25 and 37°C, b) 40:20 mM AOT:OAPB with and without salt at 25°C.

Table H.1: Diffusion coefficients of vesicles in solution.

Composition	Isotope	T [°C]	$D_{eff} \cdot 10^{10}$ [m^2/s]	Error $\cdot 10^{10}$ [m^2/s]
40 mM AOT 20 mM d-OAPB	H D	25 37	2.50 3.53	0.12 0.22
40 mM AOT 20 mM OAPB	H H	25	2.11	0.13
40 mM AOT 20 mM OAPB 20 mM NaCl	H H -	25	0.53	0.03

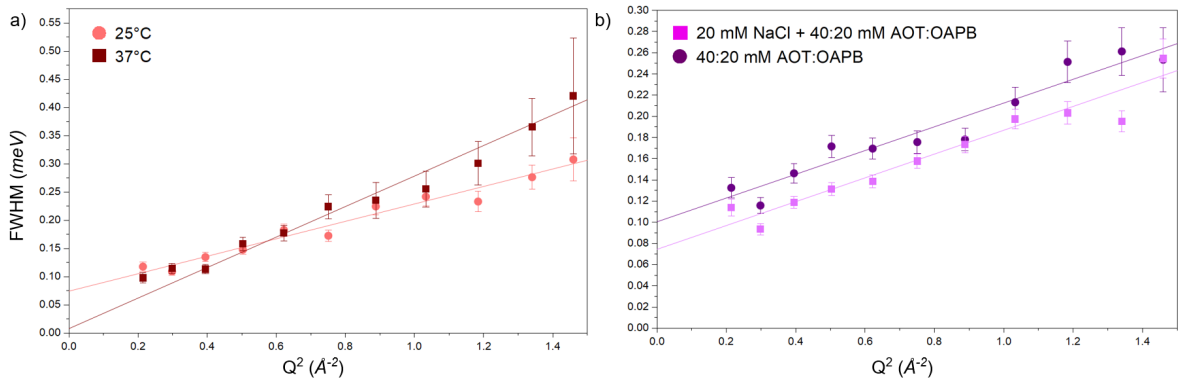

Figure H.2: Variation of the FWHM of the second Lorentzian as a function of Q^2 for a) 40:20 mM AOT:(deuterated)OAPB without salt addition at 25 and 37°C, b) 40:20 mM AOT:OAPB with and without salt at 25°C.

Table H.2: Lateral diffusion coefficients of single surfactants within the membrane layer.

Composition	Isotope	T [°C]	$D_{eff} \cdot 10^9$ [m²/s]	Error $\cdot 10^9$ [m²/s]	τ [ps]	Error [ps]
40 mM AOT 20 mM d-OAPB	H D	25	1.18	0.08	17.6	2.5
		37	2.06	0.13	159.7	389.8
40 mM AOT 20 mM OAPB	H H	25	0.85	0.07	13.1	1.3
40 mM AOT 20 mM OAPB 20 mM NaCl	H H -	25	0.83	0.06	15.0	1.4

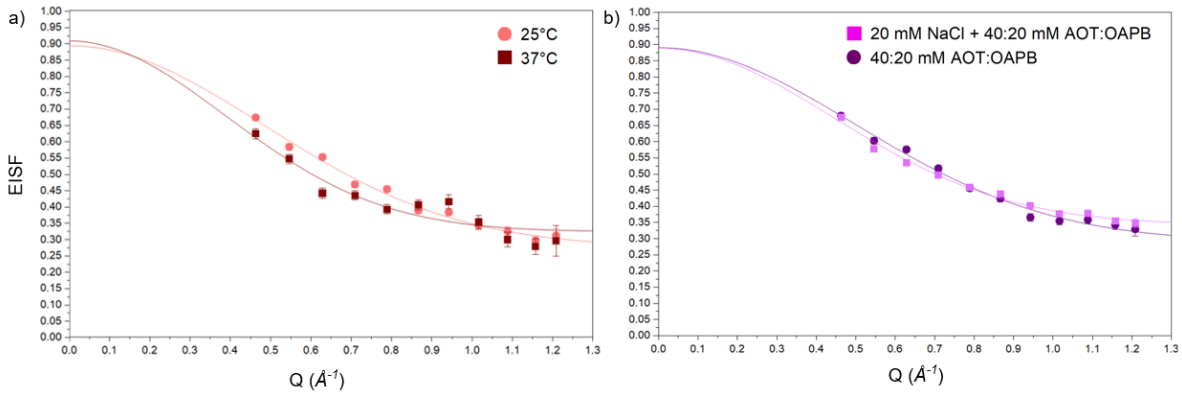

Figure H.3: Variation of the EISF as a function of Q for a) 40:20 mM AOT:(deuterated)OAPB without salt addition at 25 and 37°C, b) 40:20 mM AOT:OAPB with and without salt at 25°C.

Table H.3: Confined Gaussian model parameters.

Composition	Surfactant	T [°C]	MSD [Å^2] [Å^2]	Error [Å^2]	p	Error	A	Error
40 mM AOT 20 mM d-OAPB 20 mM NaCl	AOT	25	6.44	0.88	0.28	0.02	0.85	0.05
		37	9.92	3.10	0.33	0.02	0.86	0.20
40 mM AOT 20 mM OAPB	AOT OAPB	25	7.42	0.74	0.34	0.01	0.84	0.03
40 mM AOT 20 mM OAPB 20mM NaCl	AOT OAPB	25	6.61	0.48	0.33	0.01	0.85	0.03

QENS fitting with boundary restriction

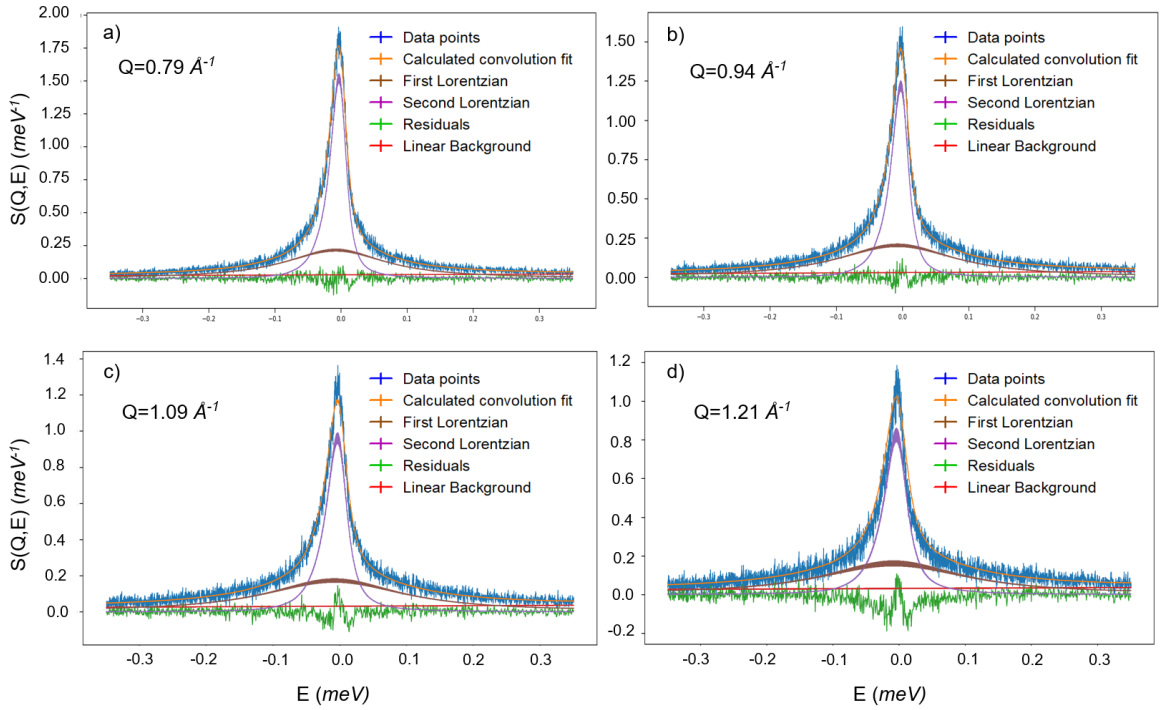

Figure I.1: Fitted QENS spectra for AOT/OAPB vesicles (40:20 mM) with the lower limit of the first Lorentzian $FWHM$ constrained. The structured residuals (green) indicate that the model does not adequately describe the experimental data.

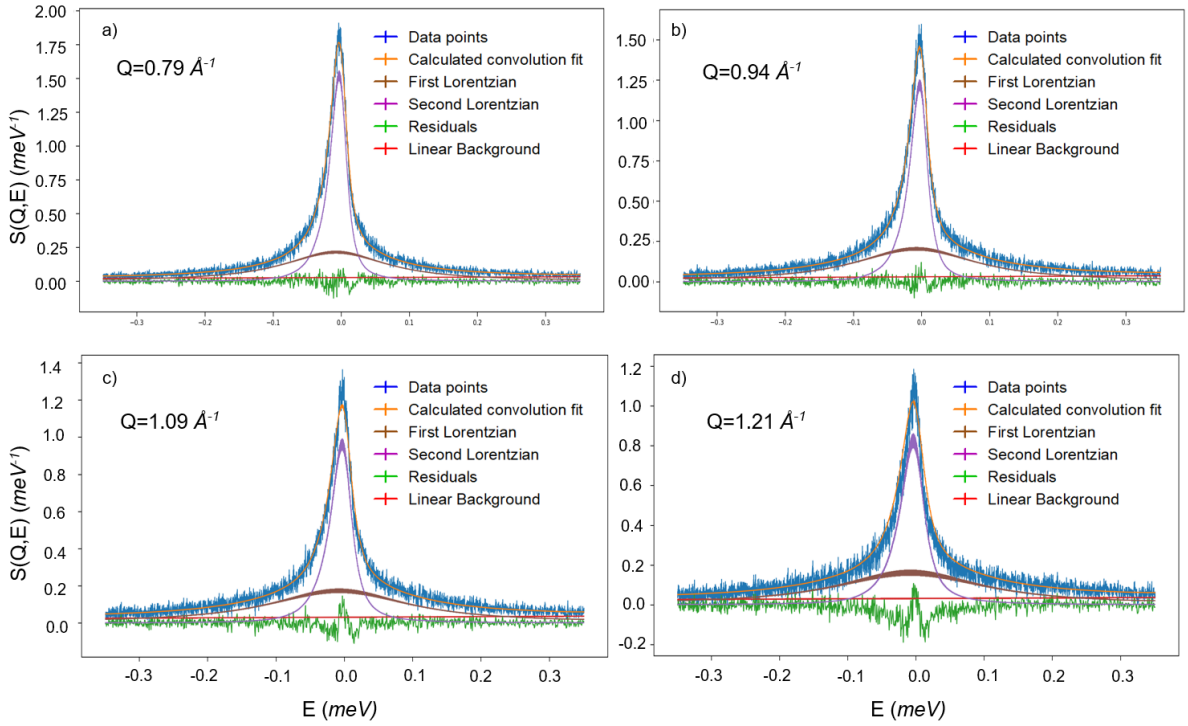

Figure I.2: Fitted QENS spectra for AOT/OAPB vesicles (40:20 mM) with the lower limit of the first Lorentzian $FWHM$ and upper limit of the Amplitude constrained. The structured residuals (green) indicate that the model does not adequately describe the experimental data.

J

Packing parameter value calculation

$$P = \frac{V_H}{a_0 l} \qquad a_0 = \pi a^2$$

$$V_H = \frac{1}{3}\pi h a^2 - \frac{1}{3}\pi (h-l) b^2$$

$$l = \frac{a-b}{b}\, h$$

$$V_H = \frac{1}{3}\pi \left(\frac{a}{a-b}\right) l a^2 - \frac{1}{3}\pi \left(\frac{b}{a-b}\right) l b^2$$

$$V_H = \frac{1}{3}\pi \frac{a^3 - b^3}{a-b}\, l = \frac{1}{3}\pi (a^2 + ab + b^2)\, l$$

$$P = \frac{V_H}{a_0 l} = \frac{\pi (a^2 + ab + b^2) l}{3 l \pi a^2} = \frac{1}{3}\left(1 + \frac{b}{a} + \frac{b^2}{a^2}\right)$$

$$P = \frac{1}{3} \Rightarrow b = 0$$

$$P = \frac{1}{2} \Rightarrow b \approx \frac{a}{3}$$

$$P = 1 \Rightarrow b = a$$

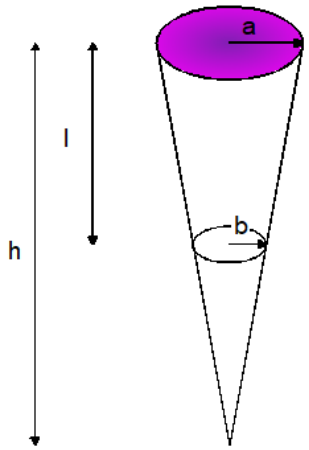

Figure J.1: Geometrical construction of P.

K

Use of AI

In this paper, AI was used to create the cover figure and to address grammatical corrections. An example of a prompt is shown below:

Q: Still in this measurements, the 20:10 mM AOT:OAPB system did not show a mixture of vesicles and ellipsoids as reported in [7]. The reason behind it could be due to different preparation methods of the samples. While in the paper the sample was prepared at the desire concentration, allowing the surfactants to aggregate ”freely”, in this work the sample was prepared by diluting the 40:20 mM AOT:OAPB solution, meaning adding solvent to a system where ellipsoid structures were already stable and formed. Thereofore to understand at which turning concentration point the repulsion due to electrostatic does not allow vesicle to form in the system due to their size, one should prepare fresh samples and analyze them, not by diluting a high concentarted solution. correct grammar

A: In these measurements, the 20:10 mM (AOT:OAPB) system did not show the coexistence of vesicles and ellipsoids as reported in [7]. This discrepancy could be attributed to differences in sample preparation methods. In the reported study, the sample was prepared directly at the desired concentration, allowing the surfactants to aggregate and organize freely. In contrast, for this work the sample was prepared by gradually diluting the 40:20 mM AOT:OAPB solution, meaning that solvent was added to a system in which ellipsoidal structures were already stable and formed. Therefore, to determine the transition concentration at which electrostatic repulsion and excluded volume effects prevent the formation of vesicles due to their bigger size, fresh samples should be prepared directly at each concentration and analyzed, rather than obtained by diluting a higher concentration solution.